Structural and functional characterization of DdrC, a novel DNA damage-induced nucleoid associated protein involved in DNA compaction

Anne-Sophie Banneville, Claire Bouthier de La Tour, Cécilia Hognon, Jacques-Philippe Colletier, Jean-Marie Teulon, Aline Le Roy, Jean-Luc Pellequer, Antonio Monari, François Dehez, Fabrice Confalonieri, et al.

Nucleic Acids Research, 2022 **1**
https://doi.org/10.1093/nar/gkac563

Structural and functional characterization of DdrC, a novel DNA damage-induced nucleoid associated protein involved in DNA compaction

Anne-Sophie Banneville[1], Claire Bouthier de la Tour[2], Salvatore De Bonis[1], Cécilia Hognon[3], Jacques-Philippe Colletier[1], Jean-Marie Teulon[1], Aline Le Roy[1], Jean-Luc Pellequer[1], Antonio Monari[3,4], François Dehez[3], Fabrice Confalonieri[2], Pascale Servant[2] and Joanna Timmins[1,*]

[1]Univ. Grenoble Alpes, CEA, CNRS, IBS, F-38000 Grenoble, France, [2]Université Paris-Saclay, CEA, CNRS, Institute for Integrative Biology of the Cell (I2BC), 91198 Gif-sur-Yvette, France, [3]LPCT, UMR 7019, Université de Lorraine, CNRS, Vandœuvre-lès-Nancy, France and [4]Université Paris Cité, CNRS, Itodys, F-75006 Paris, France

Received February 24, 2022; Revised May 18, 2022; Editorial Decision June 14, 2022; Accepted June 17, 2022

ABSTRACT

Deinococcus radiodurans **is a spherical bacterium well-known for its outstanding resistance to DNA-damaging agents. Exposure to such agents leads to drastic changes in the transcriptome of *D. radiodurans*. In particular, four *Deinococcus*-specific genes, known as DNA Damage Response genes, are strongly up-regulated and have been shown to contribute to the resistance phenotype of *D. radiodurans*. One of these, DdrC, is expressed shortly after exposure to γ-radiation and is rapidly recruited to the nucleoid. *In vitro*, DdrC has been shown to compact circular DNA, circularize linear DNA, anneal complementary DNA strands and protect DNA from nucleases. To shed light on the possible functions of DdrC in *D. radiodurans*, we determined the crystal structure of the domain-swapped DdrC dimer at a resolution of 2.5 Å and further characterized its DNA binding and compaction properties. Notably, we show that DdrC bears two asymmetric DNA binding sites located on either side of the dimer and can modulate the topology and level of compaction of circular DNA. These findings suggest that DdrC may be a DNA damage-induced nucleoid-associated protein that enhances nucleoid compaction to limit the dispersion of the fragmented genome and facilitate DNA repair after exposure to severe DNA damaging conditions.**

INTRODUCTION

Deinococcus radiodurans is a Gram-positive spherical bacterium, highly resistant to DNA-damaging agents including ionizing radiation, UV-light, desiccation and reactive oxygen species (1). Several mechanisms have been proposed to contribute to the maintenance of proteome and genome integrity in this bacterium: (i) multiple anti-oxidant strategies including a high intracellular Mn/Fe ratio (2), (ii) efficient DNA repair systems (3,4) and (iii) a highly compact nucleoid (5–7), which may limit dispersion of DNA fragments, thus easing DNA repair processes. Following exposure to ionizing radiation or desiccation, the transcriptome of *D. radiodurans* undergoes a drastic change with the up-regulation of many genes, several of which are involved in DNA repair (8). Interestingly, in *D. radiodurans*, this up-regulation has been shown to involve an SOS-independent response system, the radiation-desiccation response (RDR) regulon that is negatively regulated at the transcriptional level under normal growth conditions by the transcriptional repressor, DdrO (9–13). DdrO binds to a conserved 17 bp palindromic sequence named the radiation-desiccation response motif (RDRM), located in the promoter regions of regulated genes (10,14–16). Exposure of cells to radiation or desiccation leads to the activation of IrrE, a constitutively expressed metalloprotease, that cleaves DdrO leading to its inactivation, thereby relieving its negative control over gene expression (10,16–20).

After exposure to radiation or desiccation, four of the most up-regulated genes in the RDR regulon are *ddrA*, *ddrB*, *ddrC* and *ddrD* (8). These DNA damage response proteins (Ddr) are DNA-binding proteins specific to *Deinococcus* species. After exposure to ionizing radiation, these proteins are rapidly recruited to the nucleoid where they perform distinct functions (8,21). DdrA preferentially binds *in*

*To whom correspondence should be addressed. Tel: +33 4 57 42 86 78; Email: joanna.timmins@ibs.fr

vitro to 3′ single-stranded DNA (ssDNA) ends, protecting them from degradation by exonucleases and has thus been proposed to be part of an end-protection system (22,23). DdrB is an ssDNA-binding (SSB)-like protein that promotes single-strand annealing (SSA), thereby playing an important role in the assembly of small chromosomal fragments produced by exposure to high doses of γ-radiation (24,25). DdrB is also involved in plasmid transformation, through its SSA activity that enables the reconstitution of double-stranded DNA (dsDNA) plasmid after its internalization (25,26). Recent studies have shown that DdrD is a ssDNA binding protein that likely contributes to genome reconstitution following exposure to irradiation (27).

DdrC is a 25 kDa DNA-binding protein that is highly overexpressed shortly after irradiation and is rapidly recruited to the nucleoid, where it has been proposed to interact with damaged DNA (8,28). Interestingly, DdrC is distributed all over the nucleoid shortly after irradiation, but after 2–3 h, it forms discrete foci located at the sites of septal closure in between the newly segregated chromosomes of *D. radiodurans* (28). *In vitro* assays have shown that DdrC binds both ss- and dsDNA, with a preference for ssDNA. This protein exerts many activities upon DNA-binding, such as compaction of circular DNA, circularization of linear DNA, annealing of complementary DNA strands and protection of DNA from nucleases. These pleiotropic activities suggest that DdrC may play a role in the repair of radiation-induced DNA damage by preventing the dispersion of DNA fragments and participating in single-strand annealing.

To shed further light on the possible functions of *D. radiodurans* DdrC in the response to DNA damage, we here focused on elucidating its three-dimensional crystal structure and on characterizing its DNA binding properties using a combination of biochemical, biophysical and computational approaches. In the absence of any structures of DdrC homologues, we solved its structure *de novo* by use of the single-wavelength anomalous dispersion method (SAD). The structure reveals that DdrC is a largely α-helical protein, composed of an N-terminal winged helix-turn-helix (wHTH) motif and a C-terminal four-helix bundle, that folds as an unusual domain-swapped dimer. We reveal that DdrC possesses two asymmetric DNA binding sites exhibiting distinct DNA binding properties located on either side of the dimer and formed by motifs from both its N- and C-terminal domains. We also demonstrate that DdrC can modify the topology and induce a strong compaction of circular plasmid DNA in a concentration-dependent manner. Together these findings indicate that DdrC may be a novel DNA damage-induced nucleoid-associated protein (NAP) that is recruited to the nucleoid in response to irradiation to modulate the extent of compaction of the genome and facilitate DNA repair processes.

MATERIALS AND METHODS

Expression and purification of DdrC, DdrC-SeMet and mutant DdrCs

The *ddrC* gene (A2G07_003810) was amplified from *D. radiodurans* genomic DNA by PCR and cloned into pProEx-HtB (EMBL) expression vector for expression with a cleavable N-terminal His-tag. DdrC was expressed in *Escherichia coli* BL21(DE3) cells grown in LB supplemented with 100 $\mu g.ml^{-1}$ ampicillin. DdrC point mutants M1 to M9 were prepared by site-directed mutagenesis using the Agilent QuickChange mutagenesis protocol, the wild-type DdrC clone in pProexHtB as a template and the oligonucleotides listed in Supplementary Table S1. Mutant M10 corresponding to the N-terminally truncated DdrC missing residues 1 to 16 was PCR amplified and cloned by restriction digestion into pProexHtB (Supplementary Table S1). Expression of wild-type (WT) and mutant DdrC was induced with 1 mM IPTG at 28°C for 4 h. Cells were pelleted by centrifugation and resuspended in 40 ml lysis buffer composed of 50 mM Tris–HCl pH 7.5, 0.8 M NaCl, 5 mM $MgCl_2$, 10% (w/v) sucrose, 0.01% (v/v) triton X-100, 1 $\mu g.ml^{-1}$ DNaseI, 1 $\mu g.ml^{-1}$ lysozyme and a tablet of complete EDTA-free Protease Inhibitor Cocktail (Roche). Cells were lysed by sonication on ice for 3 min and centrifuged at 48 300 × g for 30 min. The cleared supernatant was loaded on a 5 ml HisTrap FF nickel affinity column (Cytiva), pre-equilibrated with buffer A (50 mM Tris–HCl pH 7.5, 0.8 M NaCl, 1 mM $MgCl_2$). After washing the column with buffer A, buffer A supplemented with 25 mM imidazole and buffer A supplemented with 50 mM imidazole, DdrC was eluted with a linear gradient of imidazole from 50 to 500 mM imidazole in buffer A. The fractions containing DdrC were pooled and dialyzed overnight at 4°C against buffer A supplemented with 5% (v/v) glycerol in the presence of 1:20 (w/w) TEV protease to cleave the His-tag. The His-tag itself and traces of uncleaved protein were subsequently removed by nickel affinity chromatography on 1 ml Ni-Sepharose 6 FF resin (Cytiva) pre-equilibrated in buffer A. The cleaved DdrC was recovered in the flow-through and in a 25 mM imidazole wash, and was concentrated prior to size exclusion chromatography on a Superdex 75 10/300 GL column (Cytiva) pre-equilibrated with buffer B (20 mM Tris–HCl pH 7.5, 200 mM NaCl, 5% (v/v) glycerol). Finally, DdrC was concentrated and stored at –80°C. WT DdrC was concentrated to a final concentration of 24 $mg.ml^{-1}$, while mutants were concentrated to 2–16 $mg.ml^{-1}$. For the AFM experiments, a batch of DdrC was produced following the protocol described previously, but without glycerol in the purification buffers. This 'glycerol-free' batch was stored at a concentration of 16 $mg.ml^{-1}$ at −80°C. The selenomethionine substituted DdrC (SeMet-DdrC) was produced in *E. coli* BL21(DE3) cells grown at 37°C in minimal M9 medium supplemented with 100 $\mu g.ml^{-1}$ ampicillin using a modified version of the metabolic inhibition protocol described previously (29,30). Expression was induced overnight with 1 mM IPTG at 28°C. The SeMet-DdrC protein was then purified as described for native DdrC and was stored at 20 $mg.ml^{-1}$ in buffer B at −80°C.

Crystallization of DdrC and SeMet-DdrC

Initial crystallization hits were obtained by robotic screening at the HTX lab (EMBL) using nanoliter sitting drops at 20°C (31). Crystals grew after 2–3 months in conditions containing 1.6 M ammonium sulfate and 0.1 M Tris pH 8.0 or Bicine pH 9.0. Manual crystallization screens were

then performed using the hanging-drop vapor-diffusion method in 24-well plates at 20°C. Briefly, 1 μl protein solution (at 24 mg.ml^{-1} for native DdrC or 20 mg.ml^{-1} for SeMet-DdrC) was mixed with 1 μl mother liquor solution and equilibrated against 500 μl mother liquor solution. Crystallization conditions were refined using 0.1 M Tris pH 8.0 to pH 8.5 or Bicine pH 9.0 to pH 9.5 and 1.0 M to 2.1 M ammonium sulfate. Hexagonal bipyramidal or triangular prism-shaped crystals of DdrC and SeMet-DdrC appeared after 3–4 weeks in all conditions with ammonium sulfate below 1.9 M. Crystals were transferred to mother liquor containing 20% (v/v) glycerol as a cryoprotectant and flash-cooled in liquid nitrogen before data collection. The best diffracting crystals were obtained in 0.1 M Tris pH 8.0, 1.2 M ammonium sulfate for native DdrC and 0.1 M Tris pH 8.5, 1.9 M ammonium sulfate for SeMet-DdrC.

Data collection and structure determination

A selenium single-wavelength anomalous diffraction (Se-SAD) dataset was collected on a SeMet-DdrC crystal at 100 K on beamline ID23-1 at the European Synchrotron Radiation Facility (ESRF, Grenoble, France), on a Pilatus 6M detector (Dectris) to a resolution of 2.5 Å (Table 1). A total of 500 images were collected at a wavelength of 0.978 Å with 100 ms exposure and an oscillation angle of 0.15° per frame. For the native DdrC, data collection was performed at 100 K on beamline ID30A-1/MASSIF-1 at ESRF, on a Pilatus3 2M detector (Dectris) to a resolution of 2.5 Å (Table 1). A total of 1150 images were collected at a wavelength of 0.966 Å with 220 ms exposure and an oscillation angle of 0.1° per frame. In both cases, data were integrated, indexed and scaled with XDS (32) and crystals belonged to space group $P3_221$ with unit cell parameters of $a = 111.4$ Å, $b = 111.4$ Å, $c = 104.9$ Å and $a = 111.7$ Å, $b = 111.7$ Å, $c = 105.2$ Å respectively (Table 1). The Se-SAD dataset was processed with the CRANK2 suite (33). Briefly, SHELXC (34) was used to calculate structure factor estimates from merged intensities, after what heavy-atom search was performed using SHELXD (34) and a resolution cutoff of 3.69 Å. Two selenium sites were found. The substructure refinement and phasing were performed with REFMAC5 (35), then experimental phases were improved using density modification with PARROT (36), which enabled automatic determination of the correct hand. Automatic model building and structure refinement were performed with Buccaneer (37,38) and REFMAC5 (35), and were followed by manual building in Coot (39) and refinement in PHENIX (40). The native DdrC structure was solved by molecular replacement with Phaser MR (41) using the SeMet-DdrC structure as a search model (Table 1). The DdrC structure was then refined using iterative cycles of manual building in Coot (39) and refinement in REFMAC5 (35). The final R_{work} and R_{free} are 18.3% and 24.6%, respectively. The structure of DdrC was validated in MolProbity (42) with no Ramachandran outliers (Table 1) and deposited in the Protein Data Bank with accession number 7QVB. Analysis of dimerization interface and crystal contacts was carried out using PISA (43). Electrostatic surfaces (at pH 7.5 and 200 mM NaCl) were produced by APBS (44) from structures protonated by PDB2PQR (45) after structure-based titration of protonatable residues using PROPKA (46).

DdrC structure prediction

The sequence of DdrC was submitted to AlphaFold2 (47) via the Colaboratory service from Google Research (https://colab.research.google.com/github/sokrypton/ColabFold/blob/main/beta/AlphaFold2_advanced.ipynb) and to RosettaFold (48) (https://robetta.bakerlab.org). Of note, the mmseq2 method (49,50) was employed for the multiple-sequence alignment. The first five models predicted by each program were overlaid using the *align* tool in PyMOL (51) with overall root mean square deviation (rmsd) values of 0.312–0.498 Å for RosettaFold and of 0.266–0.735 Å for AlphaFold2. The best-ranked model from AlphaFold2 in its entirety, or as isolated N- and C-terminal domains, was used as a search model (looking for either one or two copies of the protein) to phase the native crystallographic data by molecular replacement with Phaser MR (41). The top three molecular replacement solutions were then subjected to reciprocal space refinement using REFMAC5 (10 cycles) (35) and to the buccaneer pipeline in CCP4 (37).

Preparation of supercoiled plasmid DNA

Plasmid pUC19 DNA was amplified in DH5α *E. coli* cells grown in LB with 100 μg.ml^{-1} ampicillin. The supercoiled pUC19 (pUC19sc) was extracted from 100 ml overnight cultures using the NucleoBond Xtra Midi kit (Macherey-Nagel) following manufacturer's instructions. The final DNA resuspension was performed in 50 μl milli-Q water, yielding pUC19sc at a concentration of 1.5 μg.μl^{-1} (equivalent to 900 nM). The stock solution was stored at −20°C.

Atomic force microscopy

pUC19sc was diluted in milli-Q water to a final concentration of 0.5 nM for all samples. 'Glycerol-free' DdrC was diluted in milli-Q water to a final concentration of either 2, 5, 10 or 20 nM. For the protein-DNA samples, pUC19sc was incubated with DdrC for 30 min at 30°C before sample deposition on the mica sheet. Topographic data were acquired by a multimode 8 microscope equipped with a Nanoscope V controller (Bruker, Santa Barbara, USA). Before use, a freshly cleaved V-1 grade muscovite mica (Nanoandmore, Wetzlar, Germany) sheet was pre-treated with 10 μl 5 mM $NiCl_2$ and dried under nitrogen gas. 5 μl of each sample solution was deposited on the mica, after which the mica was incubated for 2 min, then dried under a gentle stream of nitrogen gas. All imaging was conducted with the PeakForce Tapping mode and ScanAsyst mode at a rate of ∼1.0 Hz; the resolution was set to either 512 or 1024 pixels per scan line. The SCANASYST-AIR HR cantilever was employed with nominal values of $k = 0.4$ N.m^{-1}, Fq = 130 kHz and tip radius = 2 nm (Bruker probes, Camarillo, CA, USA). Whenever the ScanAsyst mode was applied, a semi-manual control was on during the imaging procedure to manually adjust the set point and gain in order to reduce the tip-sample

Table 1. Crystallographic data collection and refinement statistics. Values in parentheses are for the highest resolution shell

Dataset	SeMet-DdrC	Native DdrC
Data collection parameters		
Beamline, facility	ID23-1, ESRF	MASSIF-1, ESRF
Space group	$P32_21$	$P32_21$
Cell dimensions		
a, *b*, *c* (Å)	111.4, 111.4, 104.9	111.7, 111.7, 105.2
α, β, γ (°)	90, 90, 120	90, 90, 120
Wavelength (Å)	0.979	0.966
Resolution range (Å)	36.50–2.52 (2.61–2.52)	49.34–2.50 (2.60–2.50)
Unique reflections	24 129 (1476)	26 653 (2978)
$(I)/\sigma(I)$	6.0 (0.3)	12.6 (1.1)
R_{merge}	0.093 (3.945)	0.084 (2.012)
$CC_{1/2}$ (%)	99.7 (9.8)	99.9 (47.9)
Completeness (%)	93.1 (58.0)	99.9 (99.8)
Refinement statistics		
Reflections used in refinement	24 129 (1477)	26 627 (1844)
Reflections used for R_{free}	1212 (79)	1333 (100)
R_{work}/R_{free}	0.35 (0.46)/0.36 (0.44)	0.18 (0.34)/0.25 (0.38)
Number of atoms	3250	3534
Protein	3250	3401
Ligands/ions	0	70
Water	0	71
Average *B*-factor	88.1	80.00
Protein	88.1	80.87
Ligands/ions	N/A	124.12
Water	N/A	74.16
Ramachandran		
Favored (%)	-	98.17
Allowed (%)	-	1.83
Outliers (%)	-	0.00
Rotamer outliers (%)	-	0.00
Clashscore	-	4.37
R.m.s. deviations		
Bond lengths	-	0.013
Bond angles	-	1.68
PDB accession code	-	7QVB

interactions to the minimum. The ramp size was kept constant at 150 nm. Processing of raw AFM images was systematically performed using the Gwyddion software (52). First, raw AFM images were flattened using a plane fit to the first order, then the flattening effect was further enhanced by applying the 'line flattening' tool of Gwyddion with a polynomial of order 3, followed by exclusion of all imaged objects whose height values exceeded the given threshold (usually 0.1–0.5 nm). When necessary, stripe noises were reduced using the 'Remove Scars' function in Gwyddion. Measurements of the surface areas of individual assemblies were performed on these processed AFM images corresponding to 2 μm^2 or 1 μm^2 areas. A classical height threshold was applied on the image to select as many individual assemblies as possible. Assemblies that either touched the border of the image or were not clearly identifiable due to unresolved overlapping (three or more plasmids in a single selection) were excluded from the statistical analysis. The surface areas of the selected assemblies were extracted using the grain distribution function in Gwyddion. To discriminate between the condensed or more opened assemblies, a surface area threshold of 6000–9500 nm^2 was applied to each image depending on their respective height threshold used for selection. Histograms and scatter-plots representing the fraction of condensed assemblies as a function of DdrC concentration were then plotted using the GraphPad Prism 8 software.

Fluorescence polarization

Equilibrium fluorescence polarization DNA binding assays were performed on a Clariostar (BMG Labtech) microplate reader, fitted with polarization filters. Reactions were performed in black 386-well medium-binding plates (Greiner). 0–100 μM DdrC (dimer) were titrated into 10 nM 5′-FAM labeled dsDNA 20 mer or 50 mer substrates (Table S2) in binding buffer composed of 20 mM Tris pH 8.0, 100 mM NaCl, 1 mM $MgCl_2$ and 0.2 $mg.ml^{-1}$ BSA. Reactions were performed in a final volume of 40 μl at room temperature. After subtracting the polarization values obtained for DNA alone, the mean data from at least three independent measurements were fitted to one of the following equations using GraphPad Prism 8: (a) a one-site specific binding model with Hill coefficient ($Y = (B_{max}*X^h)/(K_D{}^h + X^h)$), or (b) a two-site specific binding model ($Y = [(B_{max}(\text{Hi})*X)/(K_D(\text{Hi}) + X)] + [(B_{max}(\text{Lo})*X)/(K_D(\text{Lo}) + X)]$), where Y is the difference between the anisotropy of completely bound and completely free oligo, B_{max} is the maximal polarization signal, X is the DdrC concentration, K_D is the equilibrium dissociation constant and h is the Hill slope. The two models were compared using the Akaike's Information Criterion, AIC, implemented in GraphPad Prism 8, to determine which one the two models best fits the WT DdrC data.

Analysis of plasmid topology by 1D and 2D gel electrophoresis

200 ng of relaxed DNA (relaxed pHOT-1 DNA, 2.4 kb) (Topogen) was incubated for 15 min at 4°C in the absence or presence of increasing concentrations of DdrC in 25 μl of buffer composed of 40 mM Tris–HCl pH 7.8, 5 mM $MgCl_2$, 1.5 mM DTT, 50 mM NaCl, 12% (v/v) glycerol. 10 U of topoisomerase I from wheat germ (Sigma) was then added and the samples were incubated 30 min at 30°C. Reactions were stopped by addition of a mix of 1 mg.ml^{-1} Proteinase K and 0.5% (w/v) SDS followed by an incubation at 37°C for 10 min. 7 μl 6X DNA Loading Dye were then added to the reactions and 10 μl of the reaction mixtures were separated by gel electrophoresis at 4°C on 1.2% agarose gels in TEP buffer (36 mM Tris–HCl pH 7.8, 30 mM NaH_2PO4, 1 mM EDTA) at 4.3 V/cm for 4 h. DNA topoisomers were revealed after ethidium bromide staining. For 2D gel electrophoresis, 20 μl of the remaining reaction mixtures were loaded on a 1.2% agarose gel. The first dimension was performed as described above. The second dimension was run in a perpendicular direction at 1 V/cm for 16 h at room temperature in TEP buffer containing 3 μg.ml^{-1} chloroquine, a DNA intercalator that unwinds the double helix of a closed circular DNA, resulting in a loss of negative supercoils and formation of positive supercoils. The chloroquine was then eliminated from the gel by incubation in H_2O for 3 h and the distribution of topoisomers was visualized after ethidium bromide staining.

Size-exclusion chromatography coupled to multi-angle laser light scattering

Size exclusion chromatography (SEC) combined with multi-angle laser light scattering (MALLS), dynamic light scattering (DLS) and refractometry (RI) experiments were performed with a Superdex 200 10/300 GL size exclusion column equilibrated with Buffer C (20 mM Tris pH 7.5 and 200 mM NaCl) at room temperature. 20 μl DdrC at 16 mg.ml^{-1} was injected onto the column at 0.5 ml.min^{-1}. Online MALLS detection was performed with a miniDAWN-TREOS detector (Wyatt), DLS was recorded with a DynaPro Nanostar and RI measurements were performed with an Optilab eEX system (Wyatt).

Analytical ultracentrifugation

Sedimentation velocity experiments were performed at 42 000 rpm and 4°C, on a Beckman XLI analytical ultracentrifuge using a AN-60 Ti rotor (Beckman Coulter, Brea, USA) and double-sector cells with optical path lengths of 12 and 1.5 mm equipped with sapphire windows (Nanolytics, Potsdam, DE). Buffer C was used as a reference. Measurements were made on 1, 4 and 8 mg.ml^{-1} DdrC using absorbance at 280 nm and interference optics. Data were processed with the REDATE software (https://www.utsouthwestern.edu/labs/mbr/software/) and the parameters were determined with SEDNTERP and SEDFIT (53). Analysis of sedimentation coefficients and molecular weights were performed using SEDFIT (53) and GUSSI (54).

Molecular dynamics simulations

The domain-swapped DdrC dimer from the asymmetric unit was used as a starting model for all-atoms MD simulations after building the missing loops between helices α7 and α8 in chains A and B using the loop modelling tool in Modeller (55). Two MD simulations were performed on the apo-DdrC structure to verify the stability of the dimer and evaluate the overall dynamics of DdrC. For protein–DNA assemblies, two 25 bp DNA duplexes of random sequence were manually positioned on either side of the DdrC dimer following the positively charged grooves so as to minimize steric clashes between the DNA and protein side chains. DdrC-bound to two DNA duplexes were then used for five independent MD simulations to enhance the statistical sampling. All the macromolecular systems were explicitly hydrated in boxes of 42 000 water molecules containing 22 sodium ions to ensure the overall electrical neutrality of the unit cells. Water was represented by means of the TIP3P water model (56), whereas protein, DNA and ions were described using the amberf99 force field (57) including the bsc1 corrections for DNA (58). All setups were generated using the tleap facility of Amber Tools (59). Molecular rendering and analyses were done using VMD (60). MD simulations were performed using the massively parallel code NAMD (61). All trajectories were generated in the isobaric-isothermal ensemble, at 300 K under 1 atm using Langevin dynamics (62) (damping coefficient 1 ps^{-1}) and the Langevin piston method (63), respectively. Long-range electrostatic interactions were accounted for by means of the Particle Mesh Ewald (PME) algorithm (64). The rattle algorithm was used to constrain lengths of covalent bonds involving hydrogen atoms to their equilibrium value (65). The classical equations of motion were integrated through a time step of 4 fs using the hydrogen mass repartition strategy (66). Each molecular assay was thermalized during 15 ns, followed by 500 ns of production.

RESULTS

De novo phasing of the structure of DdrC: an unusual asymmetric domain-swapped dimer

DdrC is a protein for which no known structural homologues have been identified. We therefore solved the structure of *D. radiodurans* DdrC *de novo* by use of the single-wavelength anomalous dispersion method (SAD). We determined the structure of a selenomethionine variant of DdrC (SeMet-DdrC) by SAD and then solved the structure of native DdrC by molecular replacement using the SeMet-DdrC as a search model and refined it to 2.5 Å resolution (Table 1). The asymmetric unit contains a DdrC dimer composed of chains A and B (Figure 1A and B). Residues 5–228 of chain A and residues 4–231 of chain B were built into the electron density map. In chain A, the linker helix α8 connecting residues 158–169 was disordered and could not be modelled.

Recently, it was shown that use of artificial intelligence in programs such as AlphaFold2 (47) or RosettaFold (48) could enable prediction of protein structures to an accuracy high enough to allow phasing of crystallographic data by molecular replacement. To determine whether this would

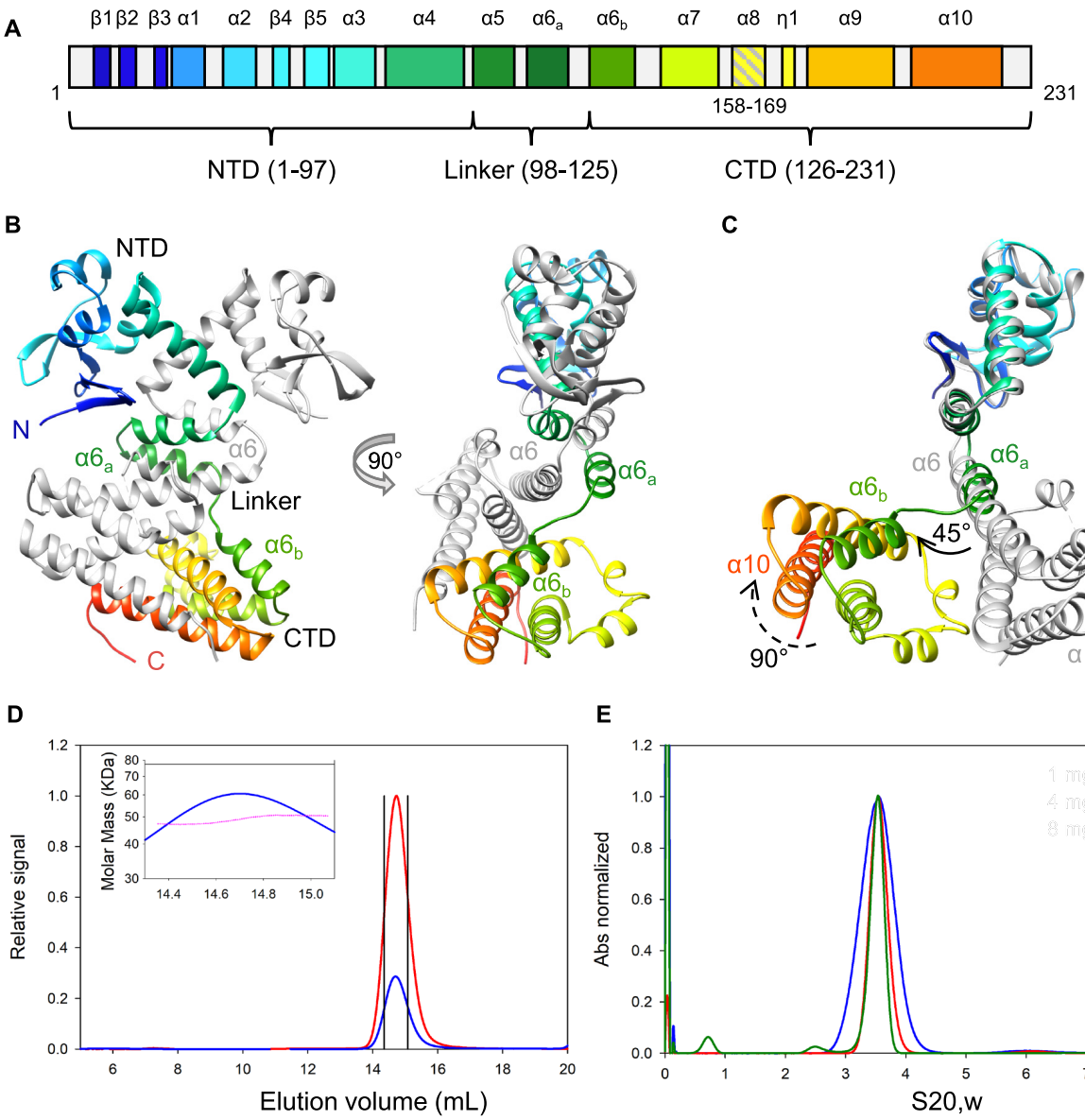

Figure 1. DdrC is an unusual domain-swapped dimer composed of two domains. (**A**) Secondary structure organization of DdrC (chain B), colored from blue (N-terminus) to orange (C-terminus). In chain A, helix α8 (residues 158 to 169) is disordered and helix α6 forms a long continuous helix. NTD: N-terminal domain, CTD: C-terminal domain. (**B**) Front and side views of the DdrC dimer, with monomer A colored in gray and monomer B colored in rainbow colors from blue (N-terminus) to red (C-terminus). The side view of DdrC highlights the asymmetry between the two faces of the dimer. (**C**) Side view of the overlay of the two DdrC chains using the NTD as a reference. Chains A and B are colored as in (**B**). The $\alpha6_a$ and $\alpha6_b$ helices in chain B correspond to a distorted conformation of the long α6 helix of chain A, probably to accommodate the domain swapping of the two monomers. (**D**) Size-exclusion chromatogram obtained from SEC-MALLS analysis of DdrC. The blue line corresponds to the refractive index and the red line to the light scattering. The inset represents a close-up view of the DdrC refractive index peak (defined by black lines), illustrating molar mass points in pink obtained along the peak. The mean mass of DdrC derived from this data was 49.1 kDa, corresponding to a dimer. (**E**) Distribution of sedimentation coefficients obtained by analytical ultracentrifugation analysis of DdrC at three concentrations: 1 mg.ml^{-1} (green), 4 mg.ml^{-1} (red) and 8 mg.ml^{-1} (blue). The normalized absorption is plotted versus $S_{20,w}$, the sedimentation coefficient corrected to 20°C in pure water. A majority of the sample (94 ± 4%) was found in a peak at a $S_{20,w}$ value of 3.55S with a mean mass of 43.5 ± 3.5 kDa from Non-Interacting Species analysis, corresponding here again to a dimer.

have been possible in the case of DdrC, we submitted the sequence of DdrC to the two programs and then attempted phasing of the native crystallographic data by molecular replacement using the best-ranked model from AlphaFold2 in its entirety or as isolated N- and C-terminal domains as a search model (see Materials and Methods for details; Supplementary Table S3 and Figure S1). Regardless of the strategy, no solution was obtained that yielded R_{free}/R_{work} values indicative of success and when these putative molecular replacement solutions were submitted to automatic model-building and refinement programs, there again, they failed to produce a reliable solution. In the case of DdrC at least, experimental phasing thus turned out to be the only route towards structure elucidation. We also attempted to predict

the dimer structure of DdrC using AlphaFold2, but none of the predicted dimer models came close to the experimentally determined structure of DdrC, likely due to the bias induced by prediction of the same monomeric structure for the two monomers in the dimer.

The asymmetric unit contains a domain-swapped homo-dimer of DdrC, in which each monomer buries on average 3262 ± 68 Å^2, corresponding to 23.5% of its surface area, within the dimer interface that is stabilized by 23 H-bonds and 10 salt bridges (43). Each monomer of DdrC is composed of two domains connected by a linker region (Figure 1A and B). The N-terminal domain (NTD; residues 1–97) comprises five β-strands and four α-helices adopting a classic winged-helix-turn-helix (wHTH) motif (β3 to β5 and α1 to α3) preceded by a β-hairpin (β1 and β2) and followed by an α-helix (α4) that provides the first contacts for dimerization. The C-terminal domain (CTD; residues 126–231), which is domain-swapped between the two monomers, is composed of four α-helices organized in a four-helix bundle motif (α6$_b$, α7, α9 and α10). Helices α7 and α9 are connected by a short helix α8, which is disordered in chain A, and a helical turn (η1). The N- and C-terminal domains are connected by a linker region comprising residues 98–125 that encompass helix α5 and the N-terminal region of α6 (α6$_a$).

Although DdrC is homo-dimeric, there is a remarkable asymmetry between the two chains, which is rarely observed in domain-swapped dimers (Figure 1C and Supplementary Table S3). The two monomers of DdrC display distinct conformations that do not overlay when the full polypeptide is considered (rmsd = 7.412 Å, Supplementary Table S3, Figure 1C). Yet, the folding of each of the two domains is conserved with the NTD, CTD and linker domains overlaying with rmsd values of 0.536, 0.870 and 4.569 Å, respectively (Supplementary Table S3). In chain A, however, the first helix of the CTD (α6) is a long uninterrupted helix ranging from residues 110 to 136, while in chain B this helix is split into two shorter helices (α6$_a$ and α6$_b$) separated by a 6-residue coil that positions α6$_b$ at a 45° angle relative to α6$_a$ helix, causing the CTD to adopt a very different orientation relative to the NTD (Figure 1C and Supplementary Figure S2). This disruption of the α6 helix in chain B is essential to accommodate the constraints of the domain-swapping. Moreover, in chain B, the CTD undergoes a further 90° rotation along the longitudinal axis of α6$_b$ that positions the helical bundle on the opposite side of the α6 helix compared to chain A (Figure 1C) and thereby allows chain B to wrap tightly around chain A, making contacts via the NTD, the linker region and the CTD (Figure 1B). As a result, the two monomers adopt very distinct conformations and this asymmetry creates a marked difference in the two faces of the dimer (Figure 1B).

A dimer of dimers was also observed by crystallographic symmetry in which two dimers face each other at a 93° angle (Supplementary Figure S3), thereby forming a putative tetramer, with a dimer-dimer interface involving mostly chain A and covering 1122 Å^2, with 14 H-bonds and eight salt bridges. We used size-exclusion chromatography coupled to multi-angle laser light scattering (SEC-MALLS) and analytical ultracentrifugation (AUC) to further characterize the quaternary structure of DdrC. Both techniques revealed that a large majority (>90%) of DdrC protein is in the form of dimers with a mass around 45 kDa (Figure 1D and E). These measurements are in agreement with earlier chemical crosslinking studies that indicated that DdrC could indeed form dimers (28). No tetramers of DdrC were detected by SEC-MALLS and AUC, suggesting that the observed tetramers most likely result from crystal packing. The biological unit thus appears to be the domain-swapped homo-dimer observed in our crystal structure.

All-atom MD simulations of the DdrC homo-dimer confirmed that the dimer was stable throughout the simulation and that the asymmetry of the dimer was also maintained, indicating that this asymmetry observed in our crystal structure does not result from crystal contacts (Supplementary Figure S4). The CTD region, with the exception of the linker between α7 and α9, and the dimer interface of DdrC are particularly stable. In the NTD, the loops and the wHTH motif exhibit some flexibility. Significant movements of the NTD with respect to the CTD were also observed allowing the wHTH of one monomer to come very close and even interact with the C-terminal four-helix bundle of the second monomer (Supplementary Figure S4).

DdrC-NTD contains a negatively charged wHTH motif

To gain insight into the potential function of DdrC, we performed a search for structural homologues of DdrC using the DALI server. The four-helix bundle in the CTD of DdrC is a very common structural motif found in diverse protein families and is thus not indicative of a particular function. The wHTH motif found in the NTD, on the other hand, has been identified as a DNA-binding motif in several proteins (67–69). The classic wHTH is a positively charged HTH motif followed by a β-hairpin, the 'wing', and preceded by a short β-strand. The conserved motif is usually folded as β-α-'turn'-α-β-'wing'-β. In most wHTH proteins, additional α-helices are packed next to the wHTH motif, usually preceding it in the sequence. In the usual DNA binding mechanism, the HTH part is inserted into the major groove of DNA while the 'wing' of the β-hairpin inserts into the minor groove.

The NTD of DdrC exhibits a classic wHTH motif (β3-α1-α2-β4-β5), although the additional α-helix (α3) is located downstream of the wHTH motif in the sequence (Figure 2A). The wHTH motif of DdrC is also preceded by a hairpin structure composed of β1 and β2. Surprisingly, the electrostatic surface potential of the NTD, calculated with the APBS program (44), indicates that the surface is mainly negatively charged, which would likely prevent DNA binding to this motif (Figure 2B). A DALI search with the NTD alone confirmed the structural homology of DdrC NTD with other wHTH-containing proteins. The proteins with the highest *Z* scores were the human Dachshund protein (PDB code 1L8R, *Z* score 7.0), the Dachshund-homology domain of human SKI protein (SKI-DHD, PDB code 1SBX, *Z* score 5.5) and *Bacillus subtilis* RacA (BsRacA, PDB code 5I44, *Z* score 4.9).

The human Dachshund protein (70) and the SKI-DHD domain (71) both of which are involved in transcriptional regulation are very similar to each other and display an unusual wHTH motif, which contains an α-helix inserted

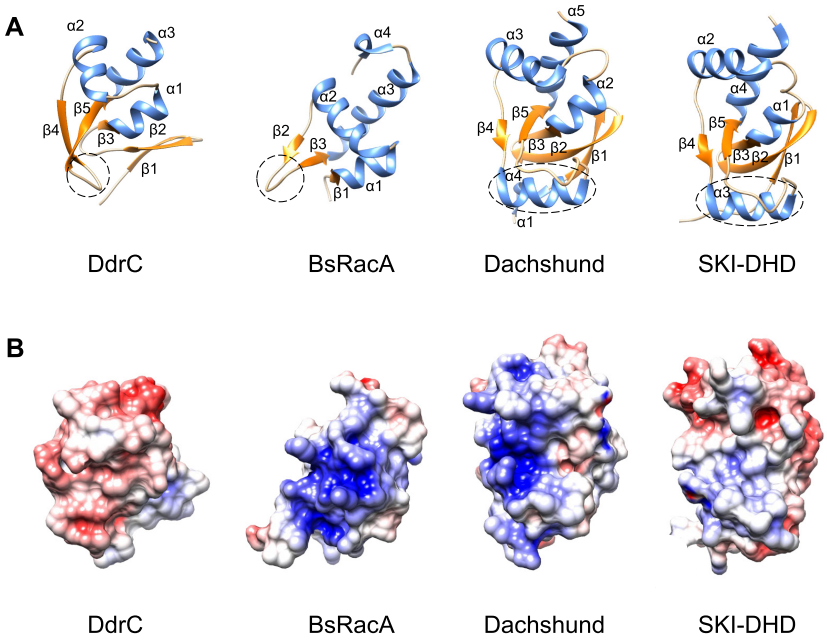

Figure 2. DdrC exhibits a classic yet negatively charged wHTH motif. (**A**) wHTH motifs of DdrC and structurally similar proteins, BsRacA (PDB code 5I44), Dachshund (PDB code 1L8R) and SKI-DHD (PDB code 1SBX). The proteins are colored based on their secondary structure, with α-helices in blue and β-sheets in orange. (**B**) DdrC, BsRacA, Dachshund and SKI-DHD are colored by electrostatic surface potential, as calculated by APBS. The color scale is the same for all proteins, ranging from −5 to + 5 kT/e, with negative charges in red and positive charges in blue.

in the β-hairpin 'wing' between β4 and β5 (β3-α2-α3-β4-α4-β5) with the adjacent α-helix located downstream in the sequence (Figure 2A). As in the case of DdrC, their wHTH motifs are preceded by a β-hairpin structure composed of the two N-terminal β-strands. However, contrary to DdrC, the wHTH motif of the Dachshund protein displays a positively charged surface, which could constitute a DNA-binding interface (70). BsRacA is a kinetochore-like chromosome-anchoring protein that possesses a more classic wHTH motif (β1-α1-α2-β2-β3) and is also positively charged (Figure 2A and B). The crystal structure of BsRacA in complex with DNA showed that the positively charged wHTH motif is directly involved in DNA binding (72). Unlike Dachshund and BsRacA, the surface of the wHTH motif of SKI-DHD is rather neutral with some electronegative patches (Figure 2B), and has been proposed to play a role in protein binding rather than in DNA binding (71). These observations suggest that the function of wHTH motifs as DNA-binding sites is more likely associated with their electrostatic surface potential than with their fold. Since the wHTH motif of DdrC exhibits a largely negatively charged surface, it is unlikely to play a direct role in DNA binding.

DdrC dimer possesses two distinct DNA binding sites

To identify a potential DNA binding site on DdrC, we analyzed the charges displayed at the surface of the DdrC dimer with the APBS program (Figure 3A). A large positive groove involving mostly arginine residues contributed by the four α-helices of the CTD and α4-α5 of the NTD is present on both sides of the dimer, suggesting that DdrC could possess two distinct DNA binding sites. To test this hypothesis, we performed fluorescence polarization assays with fluorescein-labelled dsDNA oligonucleotides of either 20 (20d5′F) or 50 (50d5′F) base-pairs. DdrC was able to bind efficiently to both DNA substrates and the experimental data were fitted to either a one-site or a two-site DNA binding model. In both cases, the fits to the two-site specific binding model were significantly better than those obtained for the simpler, one-site specific binding model (Figure 3B and C). For the 20 mer DNA, 48.0% of the DNA was bound to the high-affinity site with a K_D(Hi) of 59 nM and 52.0% of the DNA was bound to a second low-affinity site with a K_D(Lo) of 5.43 μM (Table 2). In contrast, with the longer DNA substrate (50 mer), 57.6% of the DNA was bound to the high-affinity site with a K_D(Hi) of 115 nM and 42.4% was bound to the low-affinity site with a K_D(Lo) of 91.08 μM (Table 2). These data are thus consistent with DdrC dimers possessing two distinct DNA binding sites with different affinities for the DNA that can equally accommodate short DNA strands between 20 and 50 nucleotides long. However, binding of longer DNA fragments to the low-affinity site appears to be less favorable.

Based on these observations, we built a model in which two 25 bp dsDNA fragments were bound to either face of the DdrC dimer (Figure 4A). The DNA duplexes were positioned manually along the positively charged grooves of DdrC so as to minimize steric clashes and maintain good geometry. It is interesting to note that the 25 bp dsDNA stretches all the way across these grooves, but adopts a straight conformation on one side and a more bent conformation on the other side of the DdrC dimer where the four-helix bundle of monomer A creates a bulge on the DdrC surface (Figure 4A). The robustness of this model was then verified by running five independent all-atoms MD simulations over a timescale of 500 ns each, corresponding to a total

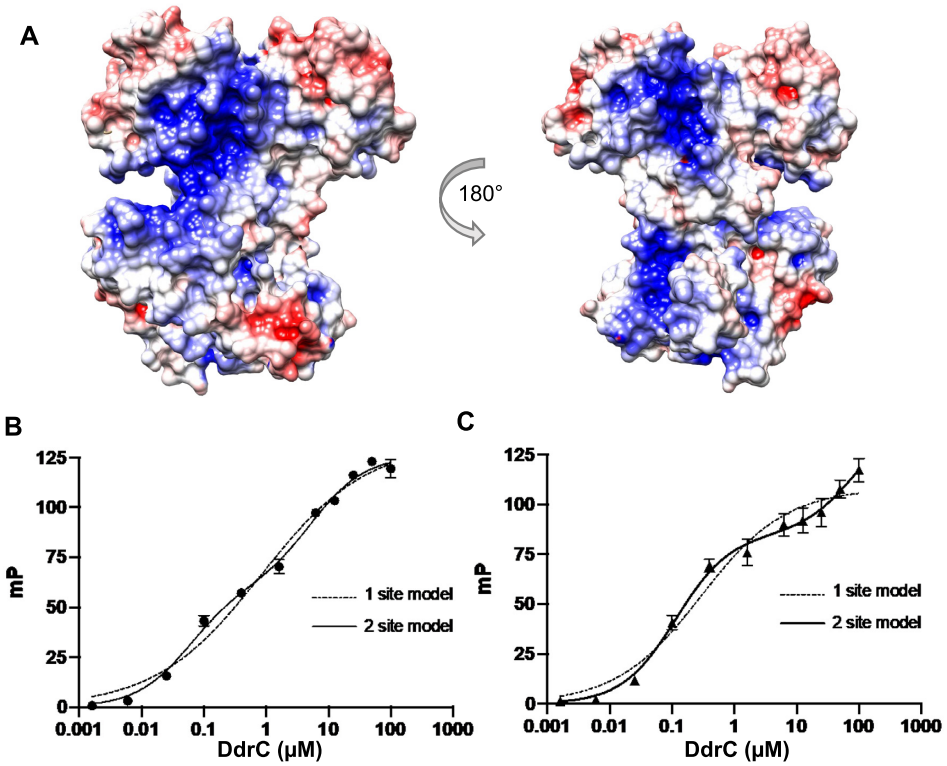

Figure 3. DdrC dimer bears two DNA-binding sites. (**A**) Depiction of the electrostatic surface potential of the DdrC dimer, as calculated by APBS. Positive and negative charges are colored in blue and red, respectively from −5 to + 5 kT/e. (B, C) Fluorescence polarization measurements of 0–100 μM DdrC binding to 10 nM 5′-FAM-labeled dsDNA oligonucleotides of 20 bp (**B**) or 50 bp (**C**). The graphs present the mean (black circles for 20 bp DNA and black triangles for 50 bp DNA) and standard deviation (SD shown as vertical error bars) of four individual polarization values recorded at each DdrC concentration. Data were fitted to one of two models using Prism 8: one-site specific binding with Hill coefficient (dashed line) and two-sites specific binding (solid line). The two fits were compared using the Akaike's Information Criterion, AIC, implemented in Prism 8, and the probability of the two-sites model being correct was determined to be >99.99% for both the 20 and 50mer dsDNAs with deltaAIC values of respectively 40.2 and 47.09.

Table 2. DNA binding constants of DdrC derived from fluorescence polarization measurements after fitting to a two-sites specific model

DNA	K_d(Hi) μM (+SEM)	K_d(Lo) μM (+SEM)	% Hi affinity	R^2
20d5′F	0.059 ± 0.009	5.435 ± 0.906	48.01 ± 2.33	0.995
50d5′F	0.115 ± 0.013	91.085 ± 57.853	57.62 ± 7.03	0.989

sampling of 2.5 μs (Figure 4B and Supplementary Figures S5 and S6 and Table S4). As in the case of DdrC alone, only minor changes in the protein conformation were observed during these simulations most of which were restricted to loop regions (Supplementary Figure S5), whereas the two DNA molecules on either side of the DdrC dimer moved substantially to adapt to the protein surface (Supplementary Figures S5 and S6). These movements of the DNA duplex include twisting, bending, sliding along the groove and rotation of the duplex to establish more favorable contacts between the minor and major grooves of the DNA molecules and the protein.

Four major contact sites between the DdrC dimer and the DNA duplexes were observed in at least four out of five MD runs (Figure 4B and C, Supplementary Table S4 and Figure S7). Interestingly, the four major contact points are all located in chain A of DdrC that interacts significantly more with the two DNA duplexes than chain B (Supplementary Table S4 and Figure S7). Both the NTD and the CTD domains of DdrC contact the DNA (Figure 4B and C). The first major contact point involves the N-terminal β-hairpin that precedes the wHTH motif located in the NTD. The second site is located in helix α4 and involves mostly Arg81. The third and fourth contact sites are located in the CTD and involve respectively Arg142 and Gln146 from helix α7 and three positively charged residues (Lys158, Arg164 and Arg167) situated in the flexible region linking helices α7 and α9. The second (Arg81) and fourth (Lys158, Arg164 and Arg167) DNA contact regions were also seen for chain B in at least three out of the five MD runs (Figure 4B and C; contact points 2′ and 4′). Each face of the DdrC dimer thus contacts a DNA duplex through at least three interaction sites, but as a result of the intrinsic asymmetry of the DdrC dimer, the contact surfaces are quite distinct (Figure 4B). The interactions between DdrC and DNA are predominantly electrostatic, between the phosphate backbone and positively charged residues, notably arginines, although additional contacts between either protein side chains or the peptide backbone and bases located in the minor groove of the DNA duplexes are also seen (Figure 4C).

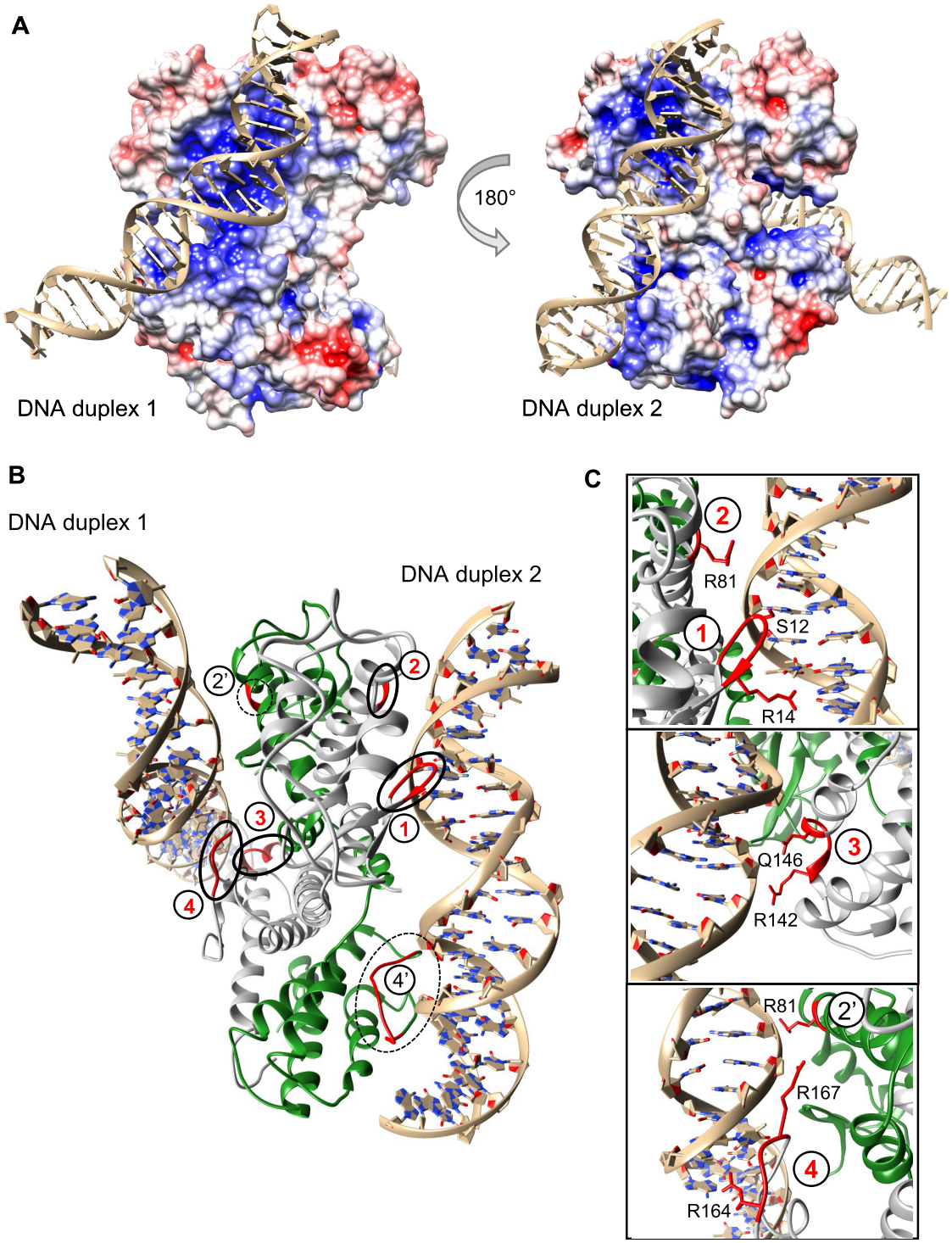

Figure 4. DdrC-dsDNA models derived from MD simulations. (**A**) Model of DNA-bound DdrC dimer used for MD simulations. Two 25 bp dsDNA fragments were manually positioned along the two positively charged grooves lining each side of the DdrC dimer. (**B**) Model of DNA-bound DdrC dimer (monomer A in grey and monomer B in green) at the end of MD simulation run3, illustrating the four major contact points (labeled 1–4 in red) and two additional contact points (labelled 2′ and 4′ in black) between the DNA duplexes and the DdrC protein. The regions of DdrC in contact with the DNA are highlighted in red. (**C**) Close-up views of the major DdrC-DNA contact sites illustrated in (**B**). The main residues involved in the interactions with the DNA are shown as sticks and are labelled.

Table 3. DNA binding constants of DdrC mutants derived from fluorescence polarization measurements after fitting to either a single site or a two-sites specific model

Mutant	Best binding model	K_d(Hi) μM (+SEM)	K_d(Lo) μM (+SEM)	% Hi affinity	R^2
WT	2 sites	0.115 ± 0.013	91.085 ± 57.853	57.62 ± 7.03	0.989
DdrC^{R142E}	2 sites	0.257 ± 0.074	61.265 ± 20.448	27.98 ± 2.22	0.981
DdrC^{K158E}	1 site	-	224.125 ± 246.998	N/A	0.991
DdrC^{R164E}	1 site	-	312.844 ± 361.794	N/A	0.981
DdrC^{R167E}	1 site	-	305.272 ± 300.850	N/A	0.988
DdrC$^{R164E/R167E}$	1 site	-	N/A (Kd > 1500)	N/A	0.885
DdrC$^{R164A/R167A}$	1 site	-	212.398 ± 341.420	N/A	0.980
DdrC^{R14E}	1 site	0.725 ± 0.101	-	N/A	0.988
DdrC^{R81E}	2 sites	0.347 ± 0.034	52.713 ± 36.977	73.56 ± 3.78	0.995
DdrC$^{del9-14S}$	2 sites	0.086 ± 0.015	12.604 ± 3.576	46.66 ± 2.52	0.992
DdrC^{delN}	1 site	1.317 ± 0.320	-	N/A	0.982

To validate these findings, we evaluated the DNA binding properties of several mutants of DdrC, listed in Supplementary Table S1. Point mutants, DdrC^{R14E}, DdrC^{R81E}, DdrC^{R142E}, DdrC^{K158E}, DdrC^{R164E}, DdrC^{R167E} and the double mutant DdrC$^{R164E/R167E}$, were prepared to exchange positively charged residues identified in our MD simulations as contacting DNA with negatively charged glutamates. In DdrC$^{R164A/R167A}$, the two arginines were mutated instead to alanine, and two N-terminally deleted constructs were also prepared to either delete entirely residues 1–16 (DdrC^{delN}) or to shorten the N-terminal β-hairpin by removing residues 9–14 and replacing them with a serine (DdrC$^{del9-14S}$). Fluorescence polarization experiments were then performed with each of these mutants to assess their binding to the fluorescein-labeled 50 mer dsDNA and the experimental data were fitted to either a single or a two-sites specific model (Supplementary Figure S8 and Table 3). Three classes of mutants could be distinguished. The first class includes DdrC$^{del9-14S}$, DdrC^{R81E} and DdrC^{R142E} mutants. These three mutants retain two distinct DNA binding sites similar to WT DdrC, with a high- and a low-affinity site (Figure 5A, Table 3 and Supplementary Figure S8). DdrC$^{del9-14S}$ shows no impaired DNA binding, indicating that the tip of the N-terminal β-hairpin is not needed for DNA binding, while DdrC^{R81E} and DdrC^{R142E} exhibit a 2- to 3-fold reduced high-affinity DNA binding site compared to WT DdrC. These two arginines are thus likely involved in DNA binding by the high-affinity site of DdrC, but are not key players in this process. The second class of mutants includes the N-terminally deleted DdrC, DdrC^{delN}, and the point mutant DdrC^{R14E}. These two mutants, in contrast to WT and class 1 mutants, exhibit only one DNA binding site, with a Kd value above 0.7 μM, i.e. 5- to 10-fold higher than the high-affinity site of WT DdrC (Figure 5B, Table 3 and Supplementary Figure S8). Class 2 mutants thus no longer exhibit a low-affinity site and show reduced binding to their high-affinity site. This suggests that the N-terminal region, and more specifically Arg14 (since the single point mutant recapitulates the effect of deleting residues 1–16), is probably implicated at least in the high-affinity site, but perhaps also in the low-affinity site. Finally, the third class of mutants involves mutations in the flexible C-terminal region connecting α7 and α9 (Figure 5C, Table 3 and Supplementary Figure S8). In these mutants (DdrC^{K158E}, DdrC^{R164E}, DdrC^{R167E}, DdrC$^{R164E/R167E}$ and DdrC$^{R164A/R167A}$), DNA binding is largely disrupted. Data were fitted to single specific binding models and the derived K_d values were over 200 μM. For the double DdrC$^{R164E/R167E}$ mutant, no reliable fit was obtained, since the binding signal was too low. This C-terminal region thus clearly constitutes the major DNA binding motif of DdrC. The high-affinity site of DdrC is thus likely formed by the tight interaction of this CTD linker, bearing Lys158, Arg164 and Arg167, from chain A with the DNA major groove of duplex 1 (contact site 4 in Figure 4B and C), which is further stabilized by contacts between Arg14 and Arg81 from chain B and Arg142 from chain A (corresponding respectively to contact points 2′ and 3 in Figure 4B and C) with the DNA. In contrast, the interaction of duplex 2 with the 'flat' surface of the DdrC dimer, notably via contact points 1 and 4′ (Figure 4B and C), likely represents the low-affinity binding site.

DdrC alters the topology of plasmid DNA

A previous study based on transmission electron microscopy showed that DdrC was able to condense circular DNA at a high concentration (28). To further investigate the effects of DdrC on plasmid conformation, we incubated supercoiled pUC19 plasmid DNA with increasing concentrations of DdrC and analyzed the resulting DNA-protein complexes by atomic force microscopy (AFM) (Figure 6 and Supplementary Figure S9). Figure 6 presents representative fields of view obtained at 0, 2, 5, 10 and 20 nM DdrC. To compare the different DNA topologies, we extracted the projected surface areas of individual plasmid-DdrC assemblies (Figure 6A–E and Supplementary Figure S9) and determined for each field of view the fraction of plasmid molecules that exhibit a condensed conformation (Figure 6F). At the highest DdrC concentration, almost all the plasmids adopted a highly condensed configuration (93 ± 13%; Figure 6E and F), which was strikingly different from the 7.5 ± 13% of condensed pUC19sc plasmid molecules in the absence of DdrC (Figure 6A and F). The fraction of condensed plasmid molecules was clearly seen to increase significantly in a DdrC concentration-dependent manner, suggesting that DdrC can maintain circular plasmid DNA in a condensed conformation.

To further explore this property of DdrC, we evaluated whether DdrC could change the topology of circular plasmid DNA by introducing either positive or negative super-

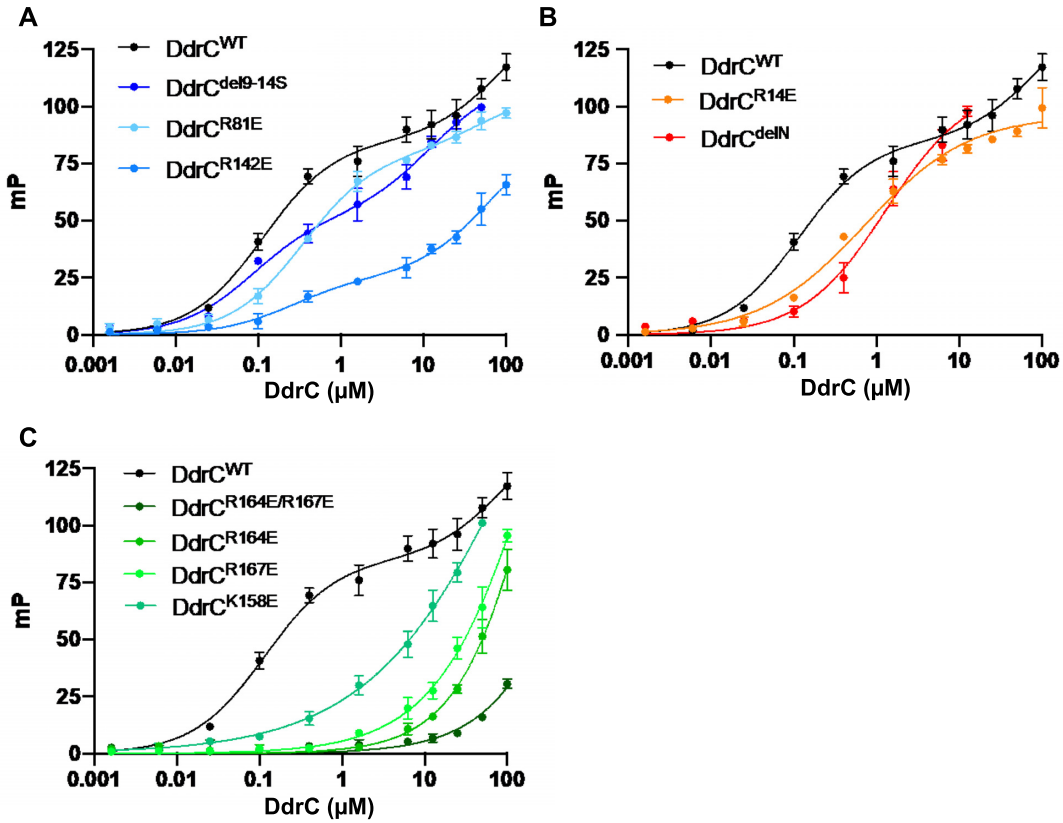

Figure 5. DNA binding curves derived from the fluorescence polarization (FP) measurements of wild-type (WT) and the three classes of DdrC mutants, class 1 (A), class 2 (B) and class 3 (C), binding to 50 bp dsDNA. The binding curve of WT DdrC is shown in black in all three panels for comparison. (**A**) Blue curves correspond to class 1 DdrC mutants ($DdrC^{del9\text{-}14S}$, $DdrC^{R81E}$ and $DdrC^{R142E}$) retaining two distinct DNA binding sites. (**B**) Red/orange curves correspond to class 2 DdrC mutants ($DdrC^{delN}$ and $DdrC^{R14E}$) having lost the second, low-affinity binding site and exhibiting reduced affinity for their high-affinity site. (**C**) Green curves correspond to DdrC mutants ($DdrC^{K158E}$, $DdrC^{R164E}$, $DdrC^{R167E}$ and $DdrC^{R164E/R167E}$) having severely impaired DNA binding properties. For reasons of clarity, the binding curve of $DdrC^{R164A/R167A}$, which is very similar to that of $DdrC^{R164E}$ is only presented in Supplementary Figure S8. Data points and associated error bars correspond respectively to the mean and standard deviation of four individual FP measurements. In all cases, the data points were fitted to either a 1-site or a 2-site binding model in GraphPad Prism 8 and the best fits are shown. DNA binding constants derived from these fits are presented in Table 3 and individual graphs are provided in Supplementary Figure S8.

coils into relaxed plasmid. For this purpose, we incubated DdrC with a relaxed circular pHOT DNA plasmid, prior to treatment with wheat germ topoisomerase I (TopoI) to relax positive or negative supercoils that might have been introduced by DdrC (Figure 7). Incubation of TopoI with the relaxed form of the plasmid had no effect on DNA topology in the absence of DdrC (Figure 7A). In contrast, when the relaxed plasmid was preincubated with DdrC prior to addition of TopoI, several additional topoisomers exhibiting increased supercoiling (faster migration) were observed indicating that DdrC is indeed able to constrain closed circular DNA in a more supercoiled conformation. To distinguish between positive and negative supercoiled topoisomers, plasmid DNA incubated with TopoI alone or with DdrC followed by TopoI were further separated by two-dimensional gel electrophoresis in the presence of chloroquine, a DNA intercalator that unwinds closed circular DNA in the second dimension (Figure 7B and Supplementary Figure S10). Interestingly, while the starting relaxed pHOT-DNA substrate migrated as slightly positively supercoiled, as expected for relaxed circular plasmid in the presence of chloroquine (73), the incubation of the substrate with increasing concentrations of DdrC generated negatively supercoiled DNA (Figure 7B and Supplementary Figure S10). DdrC is thus capable of modifying the topology of duplex DNA *in vitro* by generating negative DNA supercoils.

DISCUSSION

Our crystallographic data reveal that DdrC is composed of two domains, an unusual N-terminal wHTH motif and a more classical four-helix bundle at its C-terminus, which is domain swapped in the DdrC homo-dimer. This domain swapping is facilitated by the rearrangement of a long α-helix, α6 in chain A, into two shorter α-helices, $\alpha6_a$ and $\alpha6_b$, connected by a 6-residue linker in chain B. This break in the helix creates a highly unusual asymmetric homo-dimer, which was not predicted by current artificial intelligence programs. AlphaFold2 correctly predicted the structure of monomer A, but not of monomer B with the disrupted helix, suggesting that the monomer A conformation is likely more stable. The conformation of monomer B may only be elicited upon protein dimerization. If true, this would mean that interaction of monomer A with monomer B changes the equilibrium conformational energy landscape

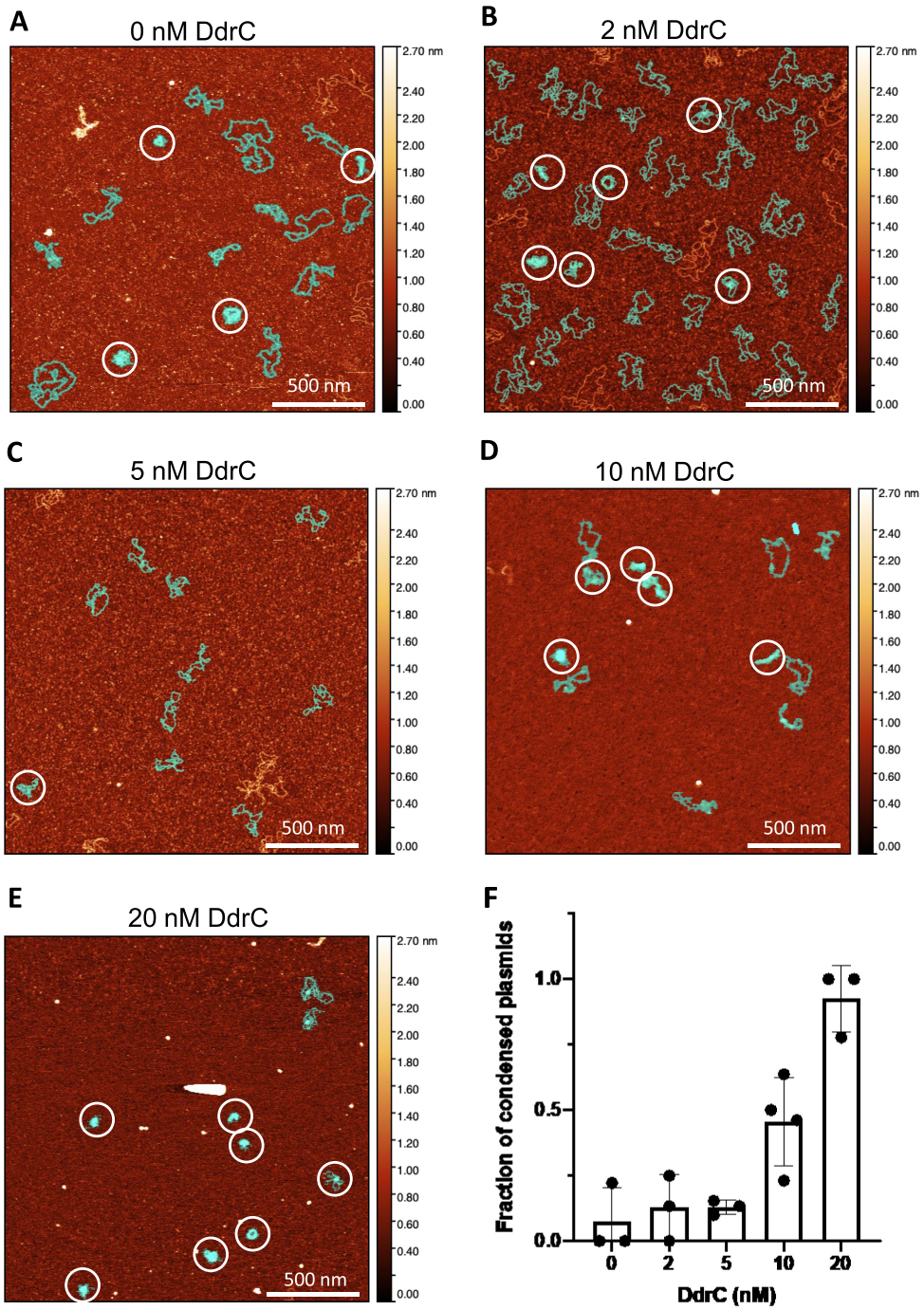

Figure 6. DdrC maintains circular plasmid in a condensed conformation. (A–E) Representative AFM images of 0.5 nM of pUC19sc incubated with 0 (**A**), 2 (**B**), 5 (**C**), 10 (**D**) and 20 nM (**E**) DdrC. Additional images are presented in Supplementary Figure S9. All images correspond to 4 μm^2 areas, in which the assemblies displaying a more condensed conformation are indicated by white circles. The light-blue/green mask highlights assemblies that have been used in the statistical analysis presented in (F). Assemblies that touch the border of the image or were not clearly identifiable due to unresolved overlapping were excluded from the statistical analysis. The z-scale bar is shown as a color gradient to indicate the distribution of height in the images. Scale bar corresponds to 500 nm. (**F**) Histogram and scatter plot illustrating the mean fraction of condensed pUC19sc-DdrC assemblies as a function of DdrC concentration. The error bars represent the standard deviation of at least three replicates. Individual data points correspond to the fraction of condensed assemblies derived from a single AFM image after estimation of the projected surface area of individual assemblies.

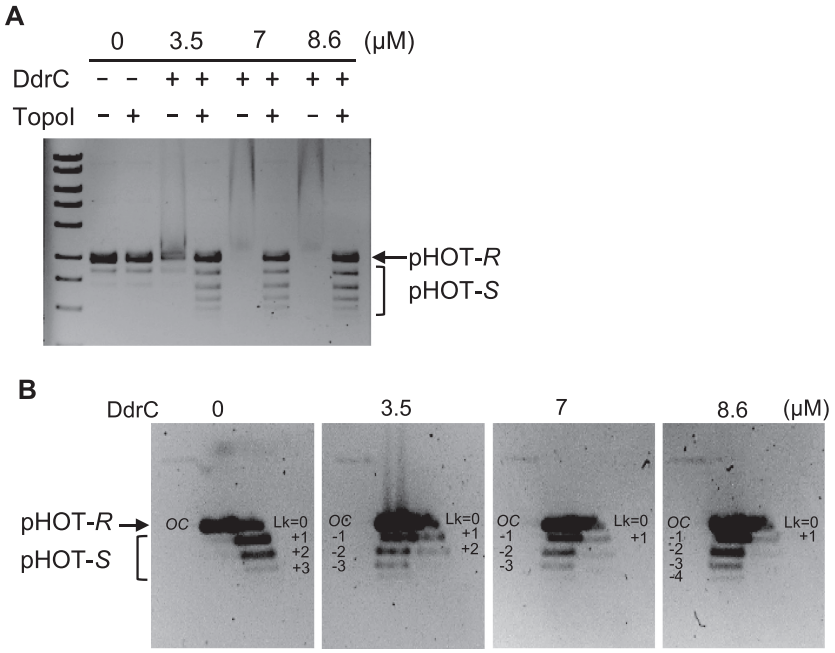

Figure 7. DdrC changes the topology of plasmid DNA by constraining DNA supercoils. (**A**) Relaxed pHOT plasmid DNA (200 ng, pHOT-*R*) incubated with 0, 3.5, 7 and 8.6 μM DdrC was then treated or not with topoisomerase I (TopoI) from wheat germ. After deproteinization, reaction products were separated by electrophoresis on a 1.2% agarose gel to resolve topoisomers. Treating relaxed plasmid DNA with TopoI has no effect, whereas treating relaxed plasmid DNA pre-incubated with 3.5–8.6 μM DdrC prior to the TopoI treatment results in a ladder-like pattern, corresponding to topoisomers exhibiting different extents of supercoiling (pHOT-*S*). (**B**) The supercoiled topoisomers resulting from DdrC and TopoI treatment were further separated by bidimensional gel with 3 μg/ml chloroquine included in the gel and buffer in the second dimension. Under these conditions, positively supercoiled topoisomers (with linking numbers of +1, +2, +3) migrate towards the right and negatively supercoiled topoisomers (with linking numbers of −1, −2, −3, −4) migrate leftwards (Supplementary Figure S10). The associated changes in linking number are indicated next to their respective bands. OC: open circular (nicked) DNA. The full gels are shown in Supplementary Figure S10.

of monomer B, leading to adoption of a new structure through inducement of a helix break and change in the relative orientation of the two domains—an impressive illustration of structural moonlighting. Alternatively, both structures may exist in solution, even though the conformation of monomer B was not predicted by the machine learning algorithms. Improvements of these algorithms in the future may allow to favor one or the other of the two hypotheses. Regardless, the DdrC dimer structure exemplifies that *de novo* phasing of crystallographic data will in some cases remain the surest pathway towards structure determination.

In DdrC, the domain swapping creates an asymmetric dimer exhibiting two distinct DNA binding surfaces. Our DdrC-DNA models suggest, however, that the conserved wHTH motif that is found in numerous DNA binding proteins is not involved in DNA binding in the case of DdrC (67–69). The electrostatic surface potential of DdrC's wHTH motif is indeed largely electronegative, precluding a direct involvement in DNA binding. The closest structural homologues of this wHTH motif of DdrC are found in the Dachsund protein (70) and the SKI-DHD domain (71), which also possess unusual wHTH motifs preceded by a N-terminal β-hairpin structure. The Dachshund protein, however, exhibits a positively charged wHTH, while the electrostatic surface potential of the SKI-DHD domain is more similar to that of DdrC and has been shown to be the site of protein–protein interactions (71). The negatively charged wHTH of DdrC may thus also constitute a binding site for a partner protein rather than for DNA.

Taken together, our fluorescence polarization measurements and MD simulations clearly indicate that DdrC can simultaneously bind two DNA duplexes via its two sides. Six potential DNA interaction sites were identified on DdrC with elements from both the NTD and the CTD taking part in DNA binding. Interestingly, in our simulations, monomer A was found to contribute significantly more than monomer B to direct contacts with the DNA (four out of the six contact points). Although each side of DdrC contacts the DNA in three different regions, the two DNA binding surfaces of DdrC are remarkably different. Our mutational study clearly shows that the high- and low-affinity binding sites identified in our fluorescence polarization experiments correspond to either side of the DdrC dimer. The flexible C-terminal linker connecting helices α7 and α9 from monomer A, in which the CTD forms a bulge on the surface, constitutes the major DNA binding motif and largely contributes to the high-affinity DNA binding site of DdrC reinforced by several additional electrostatic interactions involving both the NTD and CTD of DdrC. The low-affinity site is instead formed by the flat side of the DdrC dimer and involves the N-terminal β-hairpin motif and the CTD. Interestingly, we observed that our class 2 mutants retained DNA binding to only one site, which is likely to be the high-affinity site, albeit with reduced affinity. This suggests that either the mutated residues are involved in both binding sites on either side of the dimer, and/or that reducing the affinity to the high-affinity site leads to loss of the low-affinity site. In this scenario, the two DNA binding sites

would be tightly coupled and binding to the high-affinity site would facilitate the binding to the second low-affinity site. We do indeed observe that when the K_d for the high-affinity site increases beyond 0.5 μM (Table 3), the binding to the low-affinity site is lost, and a full disruption of the high-affinity site, as in the case of the double mutant, completely abolishes DNA binding. These observations support a model in which the two DNA binding sites are coupled and in which the binding to the second low-affinity site is likely favored by the binding of DNA to the high-affinity site, thereby increasing the local DNA concentration.

These two distinct DNA binding sites likely underlie DdrC's previously reported ability to induce the formation of loops, bridges and kinks in supercoiled plasmid DNA, DNA circularization and single-strand annealing activities (28), but also its capacity to maintain circular plasmid DNA in a condensed conformation as shown in our AFM images. This may be achieved in part at least by neutralizing the negatively charged DNA backbone to allow the close packing of DNA duplexes. In our AFM images as in earlier transmission electron micrographs of DdrC bound to DNA (28), DdrC is seen to preferentially associate with and condense single plasmid molecules and thus appears to favor binding to two sites from a given molecule rather than to two distinct plasmids, at least *in vitro*. This could be explained by the putative coupling of the high- and low-affinity sites described above that would certainly favor the binding to two regions of a given molecule rather than to two independent molecules. DNA compaction by DdrC may also be facilitated by its ability to modify the topology of circular DNA as revealed by our experiments with DdrC coupled to TopoI relaxation activity. DdrC can indeed moderately alter the topology of DNA *in vitro* by constraining negative DNA supercoils *in vitro*, an effect that has previously been reported for bacterial NAPs, such as HU or H-NS (74–76). This additional function of DdrC may be needed for the reorganization of the nucleoid in response to genotoxic stress.

Altogether these features of DdrC are reminiscent of those of classical NAPs, which play key roles in the organization and tight packaging of genomic DNA in bacterial cells through DNA bending, wrapping and bridging (77–79). The genome of *D. radiodurans* only encodes for a small number of NAPs, with HU and the DNA gyrase complex being the most abundant NAPs associated with *Deinococcus* nucleoids (21,80,81). Unlike other bacterial species, the genome of *D. radiodurans* does not encode for a classical DNA bridging NAP such as the nucleoid-structuring protein H-NS. Under normal growth conditions, the HU and DNA gyrase are thus largely responsible for maintaining the high level of compaction of *D. radiodurans* nucleoids, whilst providing sufficient plasticity to allow for the necessary rearrangements associated with cellular activity and cell cycle progression (5). Interestingly, fluorescence microscopy studies have revealed that exposure of *D. radiodurans* to high doses of γ-irradiation induces increased nucleoid compaction (28,82). Since DdrC is rapidly recruited to the nucleoid following irradiation, we propose that DdrC may function as a DNA damage-induced NAP that contributes to the enhanced level of compaction of the nucleoid after irradiation by bridging DNA duplexes, thereby limiting the dispersion of the fragmented genome immediately after irradiation to facilitate subsequent DNA repair. The DNA gyrase is also over-expressed after irradiation, and may thus also contribute to the increased nucleoid compaction observed following irradiation by modulating the extent of supercoiling of the genomic DNA, a function that may be further enhanced by the binding of DdrC to DNA and its ability to constrain DNA supercoils. The function of DdrC is likely to be, in part at least, redundant with that of other factors, such as the DNA gyrase or the HU protein, since a single deletion of *ddrC* does not significantly modify the radiation resistant phenotype of *D. radiodurans* (8,28).

Three hours post-irradiation, once the DNA repair process is almost complete (83), the abundance of DdrC decreases and the cellular distribution of DdrC changes drastically (28). DdrC which was so far evenly distributed throughout the nucleoid relocalizes to foci located near the closing septum between two *D. radiodurans* cells (28). This site corresponds to the location of the *Ter* regions of the chromosomes, where final chromosome segregation occurs, including DNA decatenation of replicated chromosomes (5,82). At this stage, the nucleoids also progressively recover their original less compacted conformation, perhaps as a result of the changes in the abundance and distribution of DdrC. This intriguing relocalization of DdrC suggests that DdrC may play a second, distinct function at the late stages of the response to DNA damage to ensure that chromosome segregation and cell division do not resume before DNA repair is complete (5,82). Further studies will be needed to explore the molecular mechanisms underlying this second putative role of DdrC in the response of *D. radiodurans* to severe radiation-induced DNA damage.

DATA AVAILABILITY

Atomic coordinates and structure factors for the reported crystal structures have been deposited with the Protein Data Bank under accession number 7QVB.

SUPPLEMENTARY DATA

Supplementary Data are available at NAR Online.

ACKNOWLEDGEMENTS

IBS acknowledges integration into the Interdisciplinary Research Institute of Grenoble (IRIG, CEA). This work used the platforms of the Grenoble Instruct-ERIC center (ISBG; UMS 3518 CNRS-CEA-UGA-EMBL) within the Grenoble Partnership for Structural Biology (PSB), supported by FRISBI (ANR-10-INBS-0005-02) and GRAL, financed within the University Grenoble Alpes graduate school (Ecoles Universitaires de Recherche) CBH-EUR-GS (ANR-17-EURE-0003). We thank Christine Ebel for access to the AUC and SEC-MALLS platforms. This work acknowledges the AFM platform at the IBS. All the calculations were performed on the local LPCT computing cluster.

FUNDING

Commissariat à l'énergie atomique et aux énergies renouvelables (CEA) through a CFR PhD grant (to A.S.B.) and a radiobiology grant; ANR (Agence Nationale de

la Recherche) and CGI (Commissariat à l'Investissement d'Avenir) are gratefully acknowledged for their financial support of this work through Labex SEAM (Science and Engineering for Advanced Materials and devices) [ANR 11 LABX 086 and ANR 11 IDEX 05 02]. Funding for open access charge: CEA Radiobiology.
Conflict of interest statement. None declared.

REFERENCES

1. Battista,J.R. (1997) Against all odds: the survival strategies of *Deinococcus radiodurans*. *Annu. Rev. Microbiol.*, **51**, 203–224.
2. Daly,M.J. (2004) Accumulation of Mn(II) in *Deinococcus radiodurans* facilitates gamma-radiation resistance. *Science*, **306**, 1025–1028.
3. Cox,M.M. and Battista,J.R. (2005) *Deinococcus radiodurans* - the consummate survivor. *Nat. Rev. Microbiol.*, **3**, 882–892.
4. Timmins,J. and Moe,E. (2016) A decade of biochemical and structural studies of the DNA repair machinery of *Deinococcus radiodurans*. *Comput. Struct. Biotechnol. J.*, **14**, 168–176.
5. Floc'h,K., Lacroix,F., Servant,P., Wong,Y.-S., Kleman,J.-P., Bourgeois,D. and Timmins,J. (2019) Cell morphology and nucleoid dynamics in dividing *Deinococcus radiodurans*. *Nat. Commun.*, **10**, 3815.
6. Levin-Zaidman,S., Englander,J., Shimoni,E., Sharma,A.K., Minton,K.W. and Minsky,A. (2003) Ringlike structure of the *Deinococcus radiodurans* genome: a key to radioresistance?*Science*, **299**, 254–256.
7. Zimmerman,J.M. and Battista,R.J. (2005) A ring-like nucleoid is not necessary for radioresistance in the *Deinococcaceae*. *BMC Microbiol.*, **5**, 17.
8. Tanaka,M., Earl,A.M., Howell,H.A., Park,M.J., Eisen,J.A., Peterson,S.N. and Battista,J.R. (2004) Analysis of *Deinococcus radiodurans*'s transcriptional response to ionizing radiation and desiccation reveals novel proteins that contribute to extreme radioresistance. *Genetics*, **168**, 21–33.
9. Blanchard,L., Guérin,P., Roche,D., Cruveiller,S., Pignol,D., Vallenet,D., Armengaud,J. and de Groot,A. (2017) Conservation and diversity of the IrrE/DdrO-controlled radiation response in radiation-resistant *Deinococcus* bacteria. *Microbiol. Open*, **6**, e00477.
10. de Groot,A., Siponen,M.I., Magerand,R., Eugénie,N., Martin-Arevalillo,R., Doloy,J., Lemaire,D., Brandelet,G., Parcy,F., Dumas,R. *et al.* (2019) Crystal structure of the transcriptional repressor DdrO: insight into the metalloprotease/repressor-controlled radiation response in *Deinococcus*. *Nucleic Acids Res.*, **47**, 11403–11417.
11. Devigne,A., Ithurbide,S., Bouthier de la Tour,C., Passot,F., Mathieu,M., Sommer,S. and Servant,P. (2015) DdrO is an essential protein that regulates the radiation desiccation response and the apoptotic-like cell death in the radioresistant *Deinococcus radiodurans* bacterium. *Mol. Microbiol.*, **96**, 1069–1084.
12. Blanchard,L. and de Groot,A. (2021) Coexistence of SOS-dependent and SOS-Independent regulation of DNA repair genes in radiation-resistant *Deinococcus* bacteria. *Cells*, **10**, 924.
13. Radman,M. (1975) SOS repair hypothesis: phenomenology of an inducible DNA repair which is accompanied by mutagenesis. *Basic Life. Sci.*, **5A**, 355–367.
14. Makarova,K.S., Omelchenko,M.V., Gaidamakova,E.K., Matrosova,V.Y., Vasilenko,A., Zhai,M., Lapidus,A., Copeland,A., Kim,E., Land,M. *et al.* (2007) *Deinococcus geothermalis*: the pool of extreme radiation resistance genes shrinks. *PLoS One*, **2**, e955.
15. Wang,Y., Xu,Q., Lu,H., Lin,L., Wang,L., Xu,H., Cui,X., Zhang,H., Li,T. and Hua,Y. (2015) Protease activity of PprI facilitates DNA damage response: Mn(2+)-dependence and substrate sequence-specificity of the proteolytic reaction. *PLoS One*, **10**, e0122071.
16. Eugénie,N., Zivanovic,Y., Lelandais,G., Coste,G., Bouthier de la Tour,C., Bentchikou,E., Servant,P. and Confalonieri,F. (2021) Characterization of the radiation desiccation response regulon of the radioresistant bacterium *Deinococcus radiodurans* by integrative genomic analyses. *Cells*, **10**, 2536.
17. Vujičić-Ž agar,A., Dulermo,R., Le Gorrec,M., Vannier,F., Servant,P., Sommer,S., de Groot,A. and Serre,L. (2009) Crystal structure of the IrrE protein, a central regulator of DNA damage repair in *Deinococcaceae*. *J. Mol. Biol.*, **386**, 704–716.
18. Ludanyi,M., Blanchard,L., Dulermo,R., Brandelet,G., Bellanger,L., Pignol,D., Lemaire,D. and de Groot,A. (2014) Radiation response in *Deinococcus deserti*: IrrE is a metalloprotease that cleaves repressor protein ddrO. *Mol. Microbiol.*, **94**, 434–449.
19. Magerand,R., Rey,P., Blanchard,L. and de Groot,A. (2021) Redox signaling through zinc activates the radiation response in *Deinococcus* bacteria. *Sci. Rep.*, **11**, 4528.
20. Narasimha,A. and Basu,B. (2021) New insights into the activation of radiation desiccation response regulon in *Deinococcus radiodurans*. *J. Biosci.*, **46**, 10.
21. Bouthier de la Tour,C., Passot,F.M., Toueille,M., Mirabella,B., Guérin,P., Blanchard,L., Servant,P., de Groot,A., Sommer,S. and Armengaud,J. (2013) Comparative proteomics reveals key proteins recruited at the nucleoid of *Deinococcus* after irradiation-induced DNA damage. *Proteomics*, **13**, 3457–3469.
22. Harris,D.R., Tanaka,M., Saveliev,S.V., Jolivet,E., Earl,A.M., Cox,M.M. and Battista,J.R. (2004) Preserving genome integrity: the DdrA protein of *Deinococcus radiodurans* R1. *PLoS Biol.*, **2**, e304.
23. Gutsche,I., Vujicic- Zagar,A., Siebert,X., Servant,P., Vannier,F., Castaing,B., Gallet,B., Heulin,T., de Groot,A., Sommer,S. *et al.* (2008) Complex oligomeric structure of a truncated form of DdrA: a protein required for the extreme radiotolerance of *Deinococcus*. *Biochim. Biophys. Acta*, **1784**, 1050–1058.
24. Xu,G., Lu,H., Wang,L., Chen,H., Xu,Z., Hu,Y., Tian,B. and Hua,Y. (2010) DdrB stimulates single-stranded DNA annealing and facilitates RecA-independent DNA repair in *Deinococcus radiodurans*. *DNA Repair (Amst.)*, **9**, 805–812.
25. Bouthier de la Tour,C., Boisnard,S., Norais,C., Toueille,M., Bentchikou,E., Vannier,F., Cox,M.M., Sommer,S. and Servant,P. (2011) The deinococcal DdrB protein is involved in an early step of DNA double strand break repair and in plasmid transformation through its single-strand annealing activity. *DNA Repair (Amst.)*, **10**, 1223–1231.
26. Ithurbide,S., Coste,G., Lisboa,J., Eugénie,N., Bentchikou,E., Bouthier de la Tour,C., Liger,D., Confalonieri,F., Sommer,S., Quevillon-Cheruel,S. *et al.* (2020) Natural transformation in *Deinococcus radiodurans*: a genetic analysis reveals the major roles of DprA, DdrB, RecA, RecF, and RecO proteins. *Front. Microbiol.*, **11**, 1253.
27. Bouthier de la Tour,C., Mathieu,M., Servant,P., Coste,G., Norais,C. and Confalonieri,F. (2021) Characterization of the DdrD protein from the extremely radioresistant bacterium *Deinococcus radiodurans*. *Extremophiles*, **25**, 343–355.
28. Bouthier de la Tour,C., Mathieu,M., Meyer,L., Dupaigne,P., Passot,F., Servant,P., Sommer,S., Le Cam,E. and Confalonieri,F. (2017) *In vivo* and *in vitro* characterization of DdrC, a DNA damage response protein in *Deinococcus radiodurans* bacterium. *PLoS One*, **12**, e0177751.
29. Doublie,S. (1997) Preparation of selenomethionyl proteins for phase determination. *Methods Enzymol.*, **276**, 523–530.
30. Timmins,J., Leiros,H.K., Leonard,G., Leiros,I. and McSweeney,S. (2005) Crystal structure of maltooligosyltrehalose trehalohydrolase from *Deinococcus radiodurans* in complex with disaccharides. *J. Mol. Biol.*, **347**, 949–963.
31. Dimasi,N., Flot,D., Dupeux,F. and Marquez,J.A. (2007) Expression, crystallization and X-ray data collection from microcrystals of the extracellular domain of the human inhibitory receptor expressed on myeloid cells IREM-1. *Acta Crystallogr. Sect. F. Struct. Biol. Cryst. Commun.*, **63**, 204–208.
32. Kabsch,W. (2010) Integration, scaling, space-group assignment and post-refinement. *Acta. Crystallogr. D Biol. Crystallogr.*, **66**, 133–144.
33. Skubák,P. and Pannu,N.S. (2013) Automatic protein structure solution from weak X-ray data. *Nat. Commun.*, **4**, 2777.
34. Sheldrick,G.M. (2010) Experimental phasing with SHELXC/D/E: combining chain tracing with density modification. *Acta. Crystallogr. D Biol. Crystallogr.*, **66**, 479–485.
35. Murshudov,G.N., Vagin,A.A. and Dodson,E.J. (1997) Refinement of macromolecular structures by the maximum-likelihood method. *Acta. Crystallogr. D Biol. Crystallogr.*, **53**, 240–255.
36. Cowtan,K. (2010) Recent developments in classical density modification. *Acta. Crystallogr. D Biol. Crystallogr.*, **66**, 470–478.

37. Cowtan,K. (2006) The buccaneer software for automated model building. 1. Tracing protein chains. *Acta. Crystallogr. D Biol. Crystallogr.*, **62**, 1002–1011.
38. Cowtan,K. (2008) Fitting molecular fragments into electron density. *Acta. Crystallogr. D Biol. Crystallogr.*, **64**, 83–89.
39. Emsley,P., Lohkamp,B., Scott,W.G. and Cowtan,K. (2010) Features and development of coot. *Acta. Crystallogr. D Biol. Crystallogr.*, **66**, 486–501.
40. Adams,P.D., Afonine,P.V., Bunkóczi,G., Chen,V.B., Davis,I.W., Echols,N., Headd,J.J., Hung,L.-W., Kapral,G.J., Grosse-Kunstleve,R.W. *et al.* (2010) PHENIX: a comprehensive Python-based system for macromolecular structure solution. *Acta. Crystallogr. D Biol. Crystallogr.*, **66**, 213–221.
41. McCoy,A.J., Grosse-Kunstleve,R.W., Adams,P.D., Winn,M.D., Storoni,L.C. and Read,R.J. (2007) Phaser crystallographic software. *J. Appl. Crystallogr.*, **40**, 658–674.
42. Chen,V.B., Arendall,W.B., Headd,J.J., Keedy,D.A., Immormino,R.M., Kapral,G.J., Murray,L.W., Richardson,J.S. and Richardson,D.C. (2010) MolProbity: all-atom structure validation for macromolecular crystallography. *Acta. Crystallogr. D Biol. Crystallogr.*, **66**, 12–21.
43. Krissinel,E. and Henrick,K. (2007) Inference of macromolecular assemblies from crystalline state. *J. Mol. Biol.*, **372**, 774–797.
44. Baker,N.A., Sept,D., Joseph,S., Holst,M.J. and McCammon,J.A. (2001) Electrostatics of nanosystems: application to microtubules and the ribosome. *Proc. Natl. Acad. Sci. U.S.A.*, **98**, 10037–10041.
45. Dolinsky,T.J., Czodrowski,P., Li,H., Nielsen,J.E., Jensen,J.H., Klebe,G. and Baker,N.A. (2007) PDB2PQR: expanding and upgrading automated preparation of biomolecular structures for molecular simulations. *Nucleic Acids Res.*, **35**, W522–W525.
46. Olsson,M.H.M., Søndergaard,C.R., Rostkowski,M. and Jensen,J.H. (2011) PROPKA3: consistent treatment of internal and surface residues in empirical pKa predictions. *J. Chem. Theory Comput.*, **7**, 525–537.
47. Jumper,J., Evans,R., Pritzel,A., Green,T., Figurnov,M., Ronneberger,O., Tunyasuvunakool,K., Bates,R., Ž ídek,A., Potapenko,A. *et al.* (2021) Highly accurate protein structure prediction with alphafold. *Nature*, **596**, 583–589.
48. Baek,M., DiMaio,F., Anishchenko,I., Dauparas,J., Ovchinnikov,S., Lee Gyu,R., Wang,J., Cong,Q., Kinch,L.N., Schaeffer,R.D. *et al.* (2021) Accurate prediction of protein structures and interactions using a three-track neural network. *Science*, **373**, 871–876.
49. Steinegger,M. and Söding,J. (2017) MMseqs2 enables sensitive protein sequence searching for the analysis of massive data sets. *Nat. Biotechnol.*, **35**, 1026–1028.
50. Mirdita,M., Steinegger,M., Breitwieser,F., Söding,J. and Levy Karin,E. (2021) Fast and sensitive taxonomic assignment to metagenomic contigs. *Bioinformatics*, **37**, 3029–3031.
51. DeLano,W.L. (2002) In: *The PyMOL molecular graphics system, version 1.8*. Schrödinger, LLC, NY.
52. Nečas,D. and Klapetek,P. (2012) Gwyddion: an open-source software for SPM data analysis. *Open Physics*, **10**, 181–188.
53. Schuck,P. (2000) Size-distribution analysis of macromolecules by sedimentation velocity ultracentrifugation and lamm equation modeling. *Biophys. J.*, **78**, 1606–1619.
54. Brautigam,C.A. (2015) Calculations and publication-quality illustrations for analytical ultracentrifugation data. *Methods Enzymol.*, **562**, 109–133.
55. Webb,B. and Sali,A. (2016) Comparative protein structure modeling using MODELLER. *Curr. Protoc. Bioinformatics*, **54**, 5.6.1–5.6.37.
56. Jorgensen,W.L., Chandrasekhar,J., Madura,J.D., Impey,R.W. and Klein,M.L. (1983) Comparison of simple potential functions for simulating liquid water. *J. Chem. Phys.*, **79**, 926–935.
57. Perez,A., Marchán,I., Svozil,D., Sponer,J., Cheatham,T.E., Laughton,C.A. and Orozco,M. (2007) Refinement of the AMBER force field for nucleic acids: improving the description of alpha/gamma Conformers. *Biophys. J.*, **92**, 3817–3829.
58. Ivani,I., Dans,P.D., Noy,A., Pérez,A., Faustino,I., Hospital,A., Walther,J., Andrio,P., Goñi,R., Balaceanu,A. *et al.* (2015) Parmbsc1: a refined force field for DNA simulations. *Nat. Methods*, **13**, 55–58.
59. Case,D.A., Cheatham,T.E., Darden,T., Gohlke,H., Luo,R., Merz,K.M., Onufriev,A., Simmerling,C., Wang,B. and Woods,R.J. (2005) The amber biomolecular simulation programs. *J. Comput. Chem.*, **26**, 1668–1688.
60. Humphrey,W., Dalke,A. and Schulten,K. (1996) VMD: visual molecular dynamics. *J. Mol. Graphics*, **14**, 33–38.
61. Phillips,J.C., Braun,R., Wang,W., Gumbart,J., Tajkhorshid,E., Villa,E., Chipot,C., Skeel,R.D., Kalé,L. and Schulten,K. (2005) Scalable molecular dynamics with NAMD. *J. Comput. Chem.*, **26**, 1781–1802.
62. Feller,S.E., Zhang,Y., Pastor,R.W. and Brooks,B.R. (1995) Constant pressure molecular dynamics simulation: the langevin piston method. *J. Chem. Phys.*, **103**, 4613–4621.
63. Martyna,G.J., Tobias,D.J. and Klein,M.L. (1994) Constant pressure molecular dynamics algorithms. *J. Chem. Phys.*, **101**, 4177–4189.
64. Darden,T., York,D. and Pedersen,L. (1993) Particle mesh ewald: an N·log(N) method for ewald sums in large systems. *J. Chem. Phys.*, **98**, 10089–10092.
65. Andersen,H.C. (1983) Rattle: a 'velocity' version of the shake algorithm for molecular dynamics calculations. *J. Comput. Phys.*, **52**, 24–34.
66. Tuckerman,M., Berne,B.J. and Martyna,G.J. (1992) Reversible multiple time scale molecular dynamics. *J. Chem. Phys.*, **97**, 1990–2001.
67. Gajiwala,K.S. and Burley,S.K. (2000) Winged helix proteins. *Curr. Opin. Struct. Biol.*, **10**, 110–116.
68. Aravind,L., Anantharaman,V., Balaji,S., Babu,M.M. and Iyer,L.M. (2005) The many faces of the helix-turn-helix domain: transcription regulation and beyond. *FEMS Microbiol. Rev.*, **29**, 231–262.
69. Teichmann,M., Dumay-Odelot,H. and Fribourg,S. (2012) Structural and functional aspects of winged-helix domains at the core of transcription initiation complexes. *Transcription*, **3**, 2–7.
70. Kim,S.-S., Zhang,R., Braunstein,S.E., Joachimiak,A., Cvekl,A. and Hegde,R.S. (2002) Structure of the retinal determination protein dachshund reveals a DNA binding motif. *Structure*, **10**, 787–795.
71. Wilson,J.J., Malakhova,M., Zhang,R., Joachimiak,A. and Hegde,R.S. (2004) Crystal structure of the dachshund homology domain of human SKI. *Structure*, **12**, 785–792.
72. Schumacher,M.A., Lee,J. and Zeng,W. (2016) Molecular insights into DNA binding and anchoring by the *Bacillus subtilis* sporulation kinetochore-like RacA protein. *Nucleic Acids Res.*, **44**, 5438–5449.
73. Gibson,E.G., Oviatt,A.A. and Osheroff,N. (2020) Two-dimensional gel electrophoresis to resolve DNA topoisomers. *Methods Mol. Biol.*, **2119**, 15–24.
74. Ghosh,S. and Grove,A. (2004) Histone-like protein HU from *Deinococcus radiodurans* binds preferentially to four-way DNA junctions. *J. Mol. Biol.*, **337**, 561–571.
75. Mukherjee,A., Sokunbi,A.O. and Grove,A. (2008) DNA protection by histone-like protein HU from the hyperthermophilic eubacterium *Thermotoga maritima*. *Nucleic Acids Res.*, **36**, 3956–3968.
76. Tupper,A.E., Owen-Hughes,T.A., Ussery,D.W., Santos,D.S., Ferguson,D.J., Sidebotham,J.M., Hinton,J.C. and Higgins,C.F. (1994) The chromatin-associated protein H-NS alters DNA topology *in vitro*. *EMBO J.*, **13**, 258–268.
77. Dame,R.T. and Tark-Dame,M. (2016) Bacterial chromatin: converging views at different scales. *Curr. Opin. Cell Biol.*, **40**, 60–65.
78. Gruber,S. (2014) Multilayer chromosome organization through DNA bending, bridging and extrusion. *Curr. Opin. Microbiol.*, **22**, 102–110.
79. Hołówka,J. and Zakrzewska-Czerwińska,J. (2020) Nucleoid associated proteins: the small organizers that help to cope with stress. *Front. Microbiol.*, **11**, 590.
80. Bouthier de la Tour,C., Blanchard,L., Dulermo,R., Ludanyi,M., Devigne,A., Armengaud,J., Sommer,S. and de Groot,A. (2015) The abundant and essential HU proteins in *Deinococcus deserti* and *Deinococcus radiodurans* are translated from leaderless mRNA. *Microbiology*, **161**, 2410–2422.
81. Chen,S.-w.W., Banneville,A.-S., Teulon,J.-M., Timmins,J. and Pellequer,J.-L. (2020) Nanoscale surface structures of DNA bound to *Deinococcus radiodurans* HU unveiled by atomic force microscopy. *Nanoscale*, **12**, 22628–22638.
82. Passot,F.M., Nguyen,H.H., Dard-Dascot,C., Thermes,C., Servant,P., Espéli,O. and Sommer,S. (2015) Nucleoid organization in the radioresistant bacterium *Deinococcus radiodurans*. *Mol. Microbiol.*, **97**, 759–774.
83. Zahradka,K., Slade,D., Bailone,A., Sommer,S., Averbeck,D., Petranovic,M., Lindner,A.B. and Radman,M. (2006) Reassembly of shattered chromosomes in *Deinococcus radiodurans*. *Nature*, **443**, 569–573.